JAERI-Tech
99-052

THERMO-MECHANICAL ANALYSIS OF AN ACCELERATION GRID FOR THE ITER-NBI SYSTEM

July 1999

Yukio FUJIWARA, Masaya HANADA,
Kenji MIYAMOTO, Yoshikazu OKUMURA,
Satoshi SUZUKI and Kazuhiro WATANABE

日本原子力研究所
Japan Atomic Energy Research Institute

本レポートは，日本原子力研究所が不定期に公刊している研究報告書です。
入手の問合わせは，日本原子力研究所研究情報部研究情報課（〒319－1195 茨城県那珂郡東海村）あて，お申し越しください。なお，このほかに財団法人原子力弘済会資料センター（〒319－1195 茨城県那珂郡東海村日本原子力研究所内）で複写による実費頒布をおこなっております。

This report is issued irregularly.
Inquiries about availability of the reports should be addressed to Research Information Division, Department of Intellectual Resources, Japan Atomic Energy Research Institute, Tokai-mura, Naka-gun, Ibaraki-ken 〒319－1195, Japan.

編集兼発行　日本原子力研究所

Thermo-mechanical Analysis of an Acceleration Grid for the ITER-NBI System

Yukio FUJIWARA, Masaya HANADA, Kenji MIYAMOTO,
Yoshikazu OKUMURA, Satoshi SUZUKI and Kazuhiro WATANABE

Department of Fusion Engineering Research
Naka Fusion Research Establishment
Japan Atomic Energy Research Institute
Naka-machi, Naka-gun, Ibaraki-ken

(Received June 8,1999)

In the engineering design of a negative ion source for the ITER-NBI system, one of the most important issues is thermo-mechanical design of acceleration grids, since excessive heat loading onto the acceleration grid could cause melting, thermal fatigue, and thermal deformation followed by beam distortion. In the present paper, thermo-mechanical characteristics of the acceleration grid were analyzed using a three-dimensional finite element code, ABAQUS, to evaluate mechanical reliability of the acceleration grid and the beam distortion. Numerical simulation indicated that the highest temperature would be about 300 °C, and that maximum von Mises equivalent stress would be about 150 MPa for a heat loading of 1.5 MW; thus, no melting on the acceleration grid would occur, while local plastic deformation would happen. To avoid the plastic deformation, it would be necessary to decrease the heat loading to less than 1 MW. Numerical simulation also indicated that maximum aperture-axis displacement due to the thermal deformation would be about 0.7 mm for the heat loading of 1.5 MW. From thin lens theory of beam optics, beamlet deflection angle by the aperture-axis displacement was estimated to be about 2 mrad, which is within the requirement of the engineering design of the ITER-NBI system.

Keywords: ITER, NBI, Acceleration Grid, Heat Loading, Numerical Simulation,
Thermal Deformation, Thin Lens Theory, Deflection Angle

ITER-NBI 用加速電極の熱・応力解析

日本原子力研究所那珂研究所核融合工学部
藤原　幸雄・花田磨砂也・宮本　賢治・奥村　義和・鈴木　哲・渡辺　和弘

（1999 年 6 月 8 日 受理 ）

加速電極への過剰な熱負荷は、電極の融解ならびに熱疲労、さらにはビーム偏向につながる電極の熱変形を引き起こす可能性がある。このため、加速電極の熱・機械設計は、ITER-NBI 用負イオン源の工学設計において最重要課題の一つである。本論文は、加速電極の熱・機械的特性を 3 次元有限要素コード(ABAQUS)を用いて解析し、加速電極の機械的信頼性ならびにビーム偏向量を評価したものである。数値解析の結果、加速電極 1 段あたりの熱負荷が 1.5MW の場合、電極の最高温度は 300℃程度、ミーゼス等価応力の最大値は 150MPa 程度になることがわかった。したがって、融解は生じないものの、加速電極の一部が塑性変形するものと予想される。塑性変形を避けるためには、熱負荷を 1MW 以下に下げる必要がある。また、数値解析から、熱変形による電極孔の最大軸ずれ量は 0.7mm 程度になることがわかった。薄型レンズ理論を適用すると、電極孔の軸ずれによるビームレットの偏向角は最大で 2 mrad 程度となり、ITER-NBI 工学設計の制限値を満たすものと評価された。

那珂研究所 ： 〒311-0193 茨城県那珂郡那珂町向山 801-1

Contents

目　次

1. Introduction

In nuclear fusion research, neutral beam injection (NBI) has been a successful scheme to heat magnetically confined plasmas.[1][2] It is also a promising candidate to drive plasma current as well as to heat a plasma in International Thermonuclear Experimental Reactor (ITER). The ITER-NBI system is designed to deliver 50 MW of 1MeV D^0 with three injector modules.[3] Each module contains a single negative ion source, which generates 1MeV D^- beams of 40 A for a duration longer than 1000 sec.[4][5] The negative ion source consists of a plasma generator, an extractor, and an accelerator, as shown in Fig. 1.1. Negative ions produced in the plasma generator are extracted with the extractor, and then accelerated up to 1 MeV in the accelerator.

During the acceleration of the negative ions, some electrons are stripped from D^- by collision with residual gas of D_2. Acceleration of the stripped electron not only reduces acceleration system efficiency, but also results in heat loading onto acceleration grids. In the engineering design of the negative ion source for the ITER-NBI system, one of the most important issues is the heat loading onto the acceleration grids. According to a three-dimensional stripping loss calculation,[6] first acceleration grid (A1G) will be subjected to a heat loading as high as 1.5 MW. The heat loading could cause serious problems, such as melting and thermal deformation of the grid, leading to water leaks and beam distortion. It is, therefore, necessary to evaluate thermo-mechanical characteristics of the acceleration grid for the engineering design of the ITER negative ion source.

The purpose of the present study is to evaluate both mechanical reliability of the acceleration grid and beam distortion due to thermal deformation. For the purpose, we analyze the acceleration grid using a three-dimensional finite element code, ABAQUS. In numerical simulation, we use two kinds of computational models: "local model" and "one-half model". Using the "local model", we calculate a part of the acceleration grid in detail to evaluate the mechanical reliability. Using the "one-half model" that is one half of a single segment of the acceleration grid, we calculate the thermal deformation of the acceleration grid to estimate aperture-axis displacement followed by the beam distortion. In the one-half model analysis, a unique method for modeling aperture regions of the grid is proposed; the method deals with the aperture regions as a material with homogeneous stiffness.

In the present paper, after a brief description of the negative ion source for the ITER-NBI system, temperature and stress distributions are calculated accurately using the local model. Then, the thermal deformation of the whole acceleration grid is estimated using the one-half model. On the basis of obtained results, beamlet deflection due to the

thermal deformation is evaluated from thin lens theory of beam optics.

2. Negative Ion Source for the ITER-NBI System

The negative ion source for the ITER-NBI system is designed to produce 1 MeV, 40 A, D^- ion beams with a current density of 20 mA/cm^2 for longer than 1000 sec. The negative ion source consists of a cesium-seeded-volume-production-type plasma generator, a multi-aperture extractor, and a multi-aperture multi-grid (MAMuG) accelerator.

The accelerator is composed of five grids forming five-acceleration stages. Each acceleration grid is divided into five segments, whose dimensions are 756 mm long, 337.5 mm wide, and 20 mm thick, as shown in Fig. 2.1. A schematic drawing of the single segment is shown in Fig. 2.2. The segment is composed of five sub-segments. The sub-segment has 52 apertures of 16 mm in diameter. Between every row of acceleration apertures, there exist rectangular channels for cooling water and permanent magnets.

3. Mechanical Reliability of the Acceleration Grid

3.1 Computational model

Figures 3.1 and 3.2 show the "local model" adopted in view of symmetry. The geometry of the local model is the same as that of the acceleration grid for the ITER-NBI system. The dimensions of the local model are 378 mm long, 11 mm wide and 20 mm thick. Figure 3.3 is a close-up view of the local model. Cooling water flows through a rectangular channel of 4.5 mm high and 3.5 mm wide. Beneath the cooling channel, there is a room for inserted permanent magnets, whose dimensions are 11 mm high and 3.5 mm wide. The material of the acceleration grid is oxygen-free-high-conductivity copper (OFHC-Cu).

In section 3, steady-state temperature distribution is calculated using material data of Tables 3.1 and 3.2. Subsequently, elastic thermal stress distribution is evaluated based on the obtained temperature distribution.

Table 3.1 Density and specific heat of OFHC-Cu

Density [kg/m^3]	8780.0
Specific heat [J/(kg · K)]	425.0

Table 3.2 Thermal conductivity of OFHC-Cu

Temperature [°C]	Thermal conductivity [W/(m · K)]
0.0	399.4
27.0	398.0
327.0	383.0
527.0	371.0

3.2 Cooling conditions in thermal analysis

Figure 3.4 shows the temperature rise of cooling water as a function of axial flow velocity at various heat-loading conditions. Heat loading onto a single acceleration grid was assumed to range from 0.5 MW to 2 MW.

We assumed an axial flow velocity of 10 m/sec as a cooling condition, since temperature rise of the cooling water is required to be less than 40 °C, which is an ITER design criterion. The flow velocity of 10 m/sec corresponds to 660 liter/min per a single acceleration grid. Using empirical equation,[7] a heat transfer coefficient was estimated to be 59,000 W/(m^2 · K).

3.3 Thermal analysis using local model

Figures 3.5 - 3.7 show finite element mesh and coordinate system of the local model. Coolant flow direction is parallel to z-axis and perpendicular to x-axis. Beam axis is parallel to y-axis.

In the thermal analysis, initial temperature of the grid was assumed to be 30 °C. Boundary conditions are shown in Fig. 3.8. Temperature rise of the cooling water along flow direction in the local model should be half magnitude of the real one, since length of the local model is half of that of the ITER acceleration grid. If inlet-water temperature is 40 °C and a heat loading is 1.5 MW, bulk temperature of cooling water through the acceleration grid increases from 40 °C to 73.2 °C. Thus, in the present analysis, bulk temperature of the local model was assumed to increase linearly from 56.6 °C to 73.2 °C.

The heat flux was assumed to concentrate on the surface around apertures, as shown in Fig. 3.9. The heated region is divided into two parts: i.e., region A and region B. The ratio of area of the regions is 10.8 % : 89.2 %. In the analysis, the ratio of the heat flux on each region was varied; three kinds of heat flux distributions, case 1, case 2, and case 3 were examined.

i) Case 1 : The ratio of the heat flux is 50 % : 50 %

For the heat loading of 1.5 MW, heat flux on the region A is 2,227 W/cm^2 and that

on the region B is 271 W/cm^2.

ii) Case 2 : The ratio of the heat flux is 100 % : 0 %.

For the heat loading of 1.5 MW, heat flux on the region A is 4,454 W/cm^2 and that on the region B is 0 W/cm^2.

iii) Case 3 : The ratio of the heat flux is 10.8 % : 89.2 %.

For the heat loading of 1.5 MW, heat flux on the region A and the region B is 483 W/cm^2.

From the viewpoint of prevention of melting, the assumption of case 2 is most severe; on the other hand, the assumption of case 3 is most mild.

Figures 3.10 - 3.12 show temperature distributions of case 1 for the heat loading of 1.5 MW. Temperature distributions of case 2 and case 3 are shown in Figs. 3.13 and 3.14, respectively. Figure 3.15 shows the highest temperature as a function of the ratio of the heat flux on the region A. For the heat loading of 1.5 MW, maximum temperature is below melting point of OFHC-Cu (1084.5 °C).

The magnitude of heat loading was changed for the heat flux distribution of case 1. Figures 3.16 and 3.17 show temperature distributions for the heat loading of 1 MW and 2 MW, respectively. The highest temperature as a function of heat loading is shown in Fig. 3.18. The highest temperature increases in proportion to heat loading.

3.4 Elastic thermal stress analysis using local model

Based on the obtained temperature distribution, elastic thermal stress distribution and deformation of the local model were calculated. The reference temperature of the local model, which is used to evaluate thermal stress, was assumed to be 30 °C. Boundary conditions are shown in Fig. 3.19. Mechanical properties of OFHC-Cu are summarized in Table 3.3.

Figure 3.20 shows finite element mesh of the local model, indicating node points and their displacement. Thermal deformation compared with the original is shown in Figs. 3.21 and 3.22. Note that the deformation is enlarged by a factor of 40 and 30, respectively.

Table 3.3 Mechanical properties of OFHC-Cu

Temperature [°C]	Elastic Modulus [GPa]	Poisson's ratio	Coefficient of Thermal Expansion [$\cdot 10^{-6}$ /K]
20.0	82.4	0.33	15.4
100.0	78.5	0.33	15.9
200.0	73.5	0.33	16.6
400.0	68.6	0.33	18.3

Maximum displacement of about 1 mm occurs at central part of the segment of the acceleration grid.

Figure 3.23 shows displacement of the central part, node 54922, in the y and z directions as a function of the ratio of the heat flux on the region A. The central-part displacement in the z direction is relatively independent of the heat flux distribution, while the displacement in the y direction is dependent on the heat flux distribution.

Figure 3.24 is a plot of the displacement as a function of heat loading, when the heat flux distribution is case 1. As can be seen from the figure, the displacement in both y and z directions increases linearly with heat loading. Figures 3.25 - 3.27 show von Mises equivalent stress distributions for the heat loading of 1.5 MW, when the heat flux distribution is case 1. Figures 3.28 and 3.29 are close-up views of von Mises equivalent stress distributions for the heat flux distribution of case 2 and case 3. Maximum von Mises equivalent stress as a function of the ratio of the heat flux on the region A is shown in Fig. 3.30. Maximum von Mises equivalent stress changes with heat flux distribution. Figure 3.31 shows yield stress of annealed OFHC-Cu as a function of temperature. [8] [9] For the heat loading of 1.5 MW, maximum von Mises equivalent stress exceeds the yield-stress level of the annealed OFHC-Cu.

The magnitude of heat loading was changed for the heat flux distribution of case 1. Figures 3.32 and 3.33 show von Mises equivalent stress distribution for the heat loading of 1 MW and 2 MW. Figure 3.34 shows maximum von Mises equivalent stress as a function of heat loading. The figure indicates that maximum von Mises equivalent stress increases with heat loading, exceeding the yield-stress level for the heat loading higher than 1 MW. Figures 3.35 - 3.40 show the stress components for the heat loading of 1.5 MW. These results indicate that thermal stress around apertures in the z direction is most severe.

3.5 Discussion

The thermal analysis indicated that the heat loading of even 1.5 MW would not cause localized melting of OFHC-Cu. However, elastic thermal stress analysis indicated that maximum von Mises equivalent stress would exceed the yield-stress level even at the heat loading of 1 MW. Cyclic stress higher than the yield stress eventually leads to low-cycle fatigue, resulting in failure. To avoid the failure, it is required to decrease the heat loading to less than 1 MW per an acceleration grid.

In the analysis, three types of heat flux distribution were examined; and then the von Mises equivalent stress distribution as well as temperature distribution proved to change greatly with the heat flux distribution. For more accurate analysis, it is desirable to measure the heat flux distribution onto the acceleration grid experimentally. For instance, it

can be measured experimentally by passing a thermal probe around an aperture of the grid in a couple of radial directions.

4. Beam Distortion due to Thermal Deformation

4.1 Computational model

The geometry of the acceleration grid is too complicated to analyze whole region of the acceleration grid accurately, so that we use a relatively large computational model of "one-half model". While the local model is just a part of the acceleration grid, the one-half model is one half of a single segment of the acceleration grid. Using the one-half model, we evaluate the thermal deformation of the segment, which may result in the beam distortion.

Figure 4.1 shows the one-half model whose dimensions are 756 mm long, 168.75 mm wide and 20 mm thick. Figure 4.2 shows detailed structure of the one-half model. Cooling water flows through seven cooling channels, which are 4.5 mm high and 3.5 mm wide. To reduce computational loading, channels for permanent magnets were ignored in the one-half model. Finite element mesh of the one-half model is shown in Fig. 4.3 with coordinate system. Similar to the local model analysis, coolant flow direction is parallel to z-axis and perpendicular to x-axis. Beam axis is parallel to y-axis.

Figure 4.4 shows "four-aperture part", which is a basic unit of aperture region. In the one-half model, aperture regions were simplified; they were supposed to be made of a homogeneous material that has equivalent stiffness of the aperture region.

In section 4, steady-state thermal analysis of the one-half model is first performed to obtain temperature distribution. Secondly, the mechanical properties of the "four-aperture part" are evaluated using its original geometry by three-dimensional simulation. Next, thermal deformation of the grid is calculated based on the obtained temperature distribution and the evaluated mechanical properties of the "four-aperture part". Finally, beamlet deflection due to the thermal deformation is evaluated using thin lens theory.

4.2 Thermal analysis using one-half model

In the thermal analysis, thermal properties of the four-aperture part were assumed to be those of OFHC-Cu. Initial temperature of the model was assumed to be 30 °C. Figure 4.5 shows boundary conditions in the thermal analysis. Coolant bulk temperature was assumed to increase linearly from 40 °C in inlet to 73.2 °C in outlet. Heat transfer coefficient was assumed to be 59,000 W/($m^2 \cdot K$). Uniform heat flux was assumed to be

injected on rectangular areas corresponding to the surfaces of the four-aperture part. The dimensions of the rectangular area are 80 mm long and 18.5 mm wide. The heat flux of 3.12 MW/m^2 corresponds to the total heat loading of 1.5 MW. Figures 4.6 and 4.7 show the temperature distributions for the heat loading of 1.5 MW. Temperature of almost all the acceleration grid is higher than 60 °C, and temperature near outlet is about 90 °C.

4.3 Mechanical properties of "four-aperture part"

Elastic modulus and Poisson's ratio of "four-aperture part"

To evaluate the mechanical properties of the four-aperture part as a unit, shown in Fig. 4.4, three-dimensional elastic simulations were performed. Figure 4.8 shows the finite element mesh of the four-aperture part with coordinate system. The four-aperture part is 80 mm long, 18.5 mm wide and 20 mm thick. Boundary conditions for elastic stress analysis are shown in Figs. 4.9, 4.11, and 4.13. Pressure of 100 MPa was assumed in each case. For example, in Fig. 4.9, the pressure was applied on the y'z' plane at x'=80 mm along x'-axis.

Figures 4.10, 4.12, and 4.14 show deformations of the four-aperture part, indicating elastic modulus in each direction. Poisson's ratio in each direction was also calculated from each displacement of the model. Evaluated equivalent elastic modulus and poisson's ratio of the four-aperture part are summarized in Tables 4.1 and 4.2.

Table 4.1 Evaluated elastic modulus of the four-aperture part

Temperature [°C]	Elastic Modulus x'-x' [GPa]	Elastic Modulus y'-y' [GPa]	Elastic Modulus z'-z' [GPa]
50.0	19.7	23.9	81.0
100.0	19.1	23.2	78.7
200.0	17.9	21.7	73.5
300.0	17.3	22.3	71.2

Table 4.2 Evaluated poisson's ratio of the four-aperture part

Temperature [°C]	Poisson's ratio x'-y'	Poisson's ratio x'-z'	Poisson's ratio y'-z'
50.0	0.098	0.131	0.199
100.0	0.098	0.131	0.199
200.0	0.098	0.131	0.200
300.0	0.098	0.131	0.213

Shear modulus

Figures 4.15, 4.17, and 4.19 show boundary conditions to evaluate shear modulus in each direction, indicating representative nodes whose displacement is checked. Shear stress of 1 MPa was assumed on a plane in each simulation.

Figures 4.16, 4.18, and 4.20 show both original and deformed mesh with the displacement of the checked nodes. From the displacement, the shear modulus was calculated in each direction. Evaluated shear modulus is summarized in Table 4.3.

4. 4 Elastic thermal stress analysis using one-half model

To evaluate the thermal deformation as a whole segment of the acceleration grid, elastic thermal stress analysis was performed based on the obtained temperature distribution and evaluated mechanical properties of the four-aperture part. The reference temperature was assumed to be 30 °C. Figure 4.21 shows the one-half model, indicating boundary conditions for the elastic thermal stress analysis.

Figure 4.22 shows thermal deformation exaggerated by a factor of 100. Figure 4.23 shows node points and their displacement for the heat loading of 1.5 MW. The corner of aperture region approximately corresponds to positions of node 14669 and node 17063. The maximum aperture-axis displacement in the z direction is approximately 0.7 mm, occurring around the node 14669, and that in the x direction is about 0.135 mm, occurring around the node 17063. Figure 4.24 shows the maximum displacement in the x and z directions as a function of heat loading. The maximum displacement increases with heat loading.

4.5 Discussion

Thermal deformation in an acceleration grid causes aperture-axis displacement, leading to beamlet deflection. As shown in Fig. 4.23, the maximum displacement occurs around the corner of aperture area, so that beamlets passing through around the corner of

Table 4.3 Evaluated shear modulus of the four-aperture part

Temperature [°C]	Shear Modulus x'-y' [MPa]	Shear Modulus x'-z' [MPa]	Shear Modulus y'-z' [MPa]
50.0	26.7	31.2	69.4
100.0	25.9	30.2	67.3
200.0	24.2	28.3	63.0
300.0	23.4	27.4	60.9

aperture area are most deflected.

In accordance with thin lens theory of beam optics, deflection angle of a beamlet θ is given as follows:

$$\theta = \frac{E\delta}{4V} \qquad (4\text{-}1)$$

where θ is deflection angle of a beamlet [rad],
E is electric field [V/m] ,
δ is aperture-axis displacement [m],
V is beam energy [eV].

We assumed that first acceleration grid (A1G) would be subjected to the heat loading ranging from 1 MW to 2 MW. Gap length and the maximum voltage between an extractor and the first acceleration grid (A1G) is 85 mm and 200 kV, respectively; electric field E is $200\times10^{3}/85\times10^{-3}$ V/m. Table 5.1 shows maximum deflection angle calculated from the thin lens theory. For the heat loading of 1.5 MW, the maximum deflection angle was estimated to be about 2 mrad. The maximum deflection angle of 2 mrad is acceptable for the ITER-NBI system, since allowable alignment of each beamlet is less than 2 mrad in the engineering design of the ITER-NBI system.[10]

5. Summary

In the engineering design of the ITER-NBI system, the influence of heat loading onto the acceleration grids is one of the most important issues. Then, we evaluated mechanical reliability and thermal deformation of the acceleration grid using numerical simulation. The simulation indicated that no melting on the acceleration grid would occur for the heat loading of 1.5 MW, while local plastic deformation would happen around apertures for the heat loading higher than about 1 MW. It would, therefore, be necessary to reduce the heat loading onto the acceleration grid to less than 1 MW so as to avoid the plastic deformation. The simulation also indicated that maximum aperture-axis

Table 5.1 Maximum deflection angle evaluated from thin lens theory

Heat loading [MW]	Maximum displacement [mm]	Deflection angle [mrad]
1.0	0.50	1.5
1.5	0.70	2.1
2.0	0.91	2.7

displacement would be about 0.7 mm for the heat loading of 1.5 MW. From the thin lens theory of beam optics, maximum beamlet deflection angle due to the aperture-axis displacement was evaluated to be about 2 mrad. It is within the requirement of the engineering design of the ITER-NBI system.

Acknowledgment

This report has been prepared as an account of work assigned to the Japanese Home Team under Task Agreement number N 53 TD 12 FJ within the Agreement among the European Atomic Energy Community, the Government of Japan, the Government of the Russian Federation, and the Government of the United States of America on Cooperation in the Engineering Design Activities for the International Thermonuclear Experimental Reactor ("ITER EDA Agreement") under the auspices of the International Atomic Energy Agency (IAEA).

We would like to express our sincere thanks to Dr. M. Ohta and Dr. S. Matsuda for their support and encouragement. We would like to acknowledge other members of NBI heating laboratory for their valuable discussions and comments. We are also grateful to Dr. P. L. Mondino, Dr. E. Di Pietro, and Dr. T. Inoue for their encouragement and valuable information.

References

[1] JT-60 Team presented by M.Kikuchi: 15th Int. Conf. on Plasma Physics and Controlled Nuclear Fusion Research, Sevilla, Spain (1994) A-1-I-2

[2] K. M McGrire, et al.: The Physics of Plasma, Special Issue (1995)

[3] ITER EDA Final Design Report, DDD 5.3, NB H&CD system

[4] R. Hemsworth et al.: Proc. 16th IAEA Fusion Energy Conference,927 (1996)

[5] R. Hemsworth et al: Rev. Sci. Instrum. 67 (3), 1120 (1996)

[6] M. Hanada et al: 16th Symp. Fus. Eng., Illinois, USA (1995)

[7] Gnielinski, V. Chem. Eng., 16-2, (1976), 359

[8] R. Wells et al: JAERI-M 84-011

[9] ASM, Metals Handbook, 9th ed., 1 278

[10] Design Description Document, Neutral Beam Heating & Current Drive System, WBS 5.3, November 28 (1997)

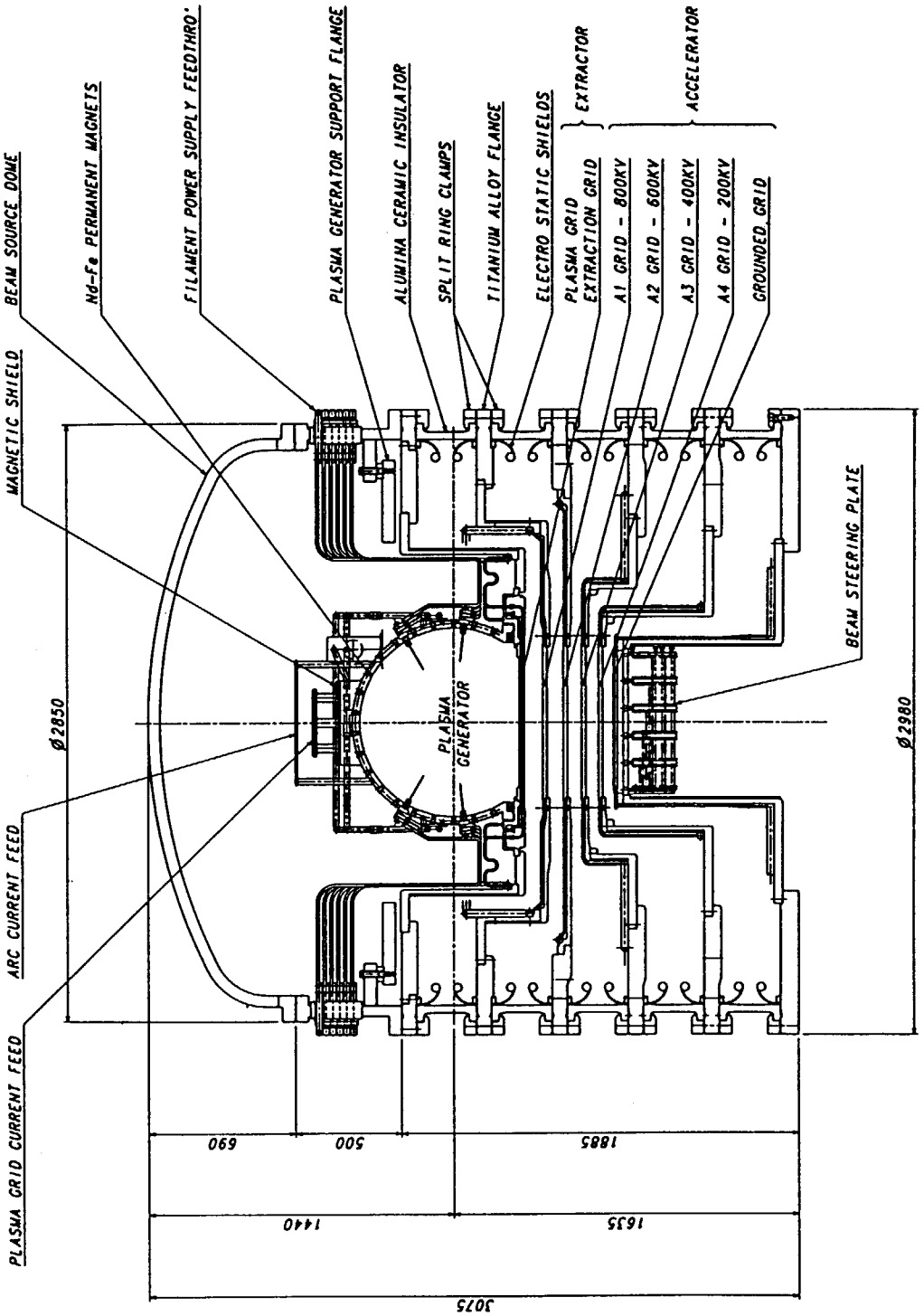

Figure 1.1 Cross sectional view of a negative ion source for the ITER-NBI system.

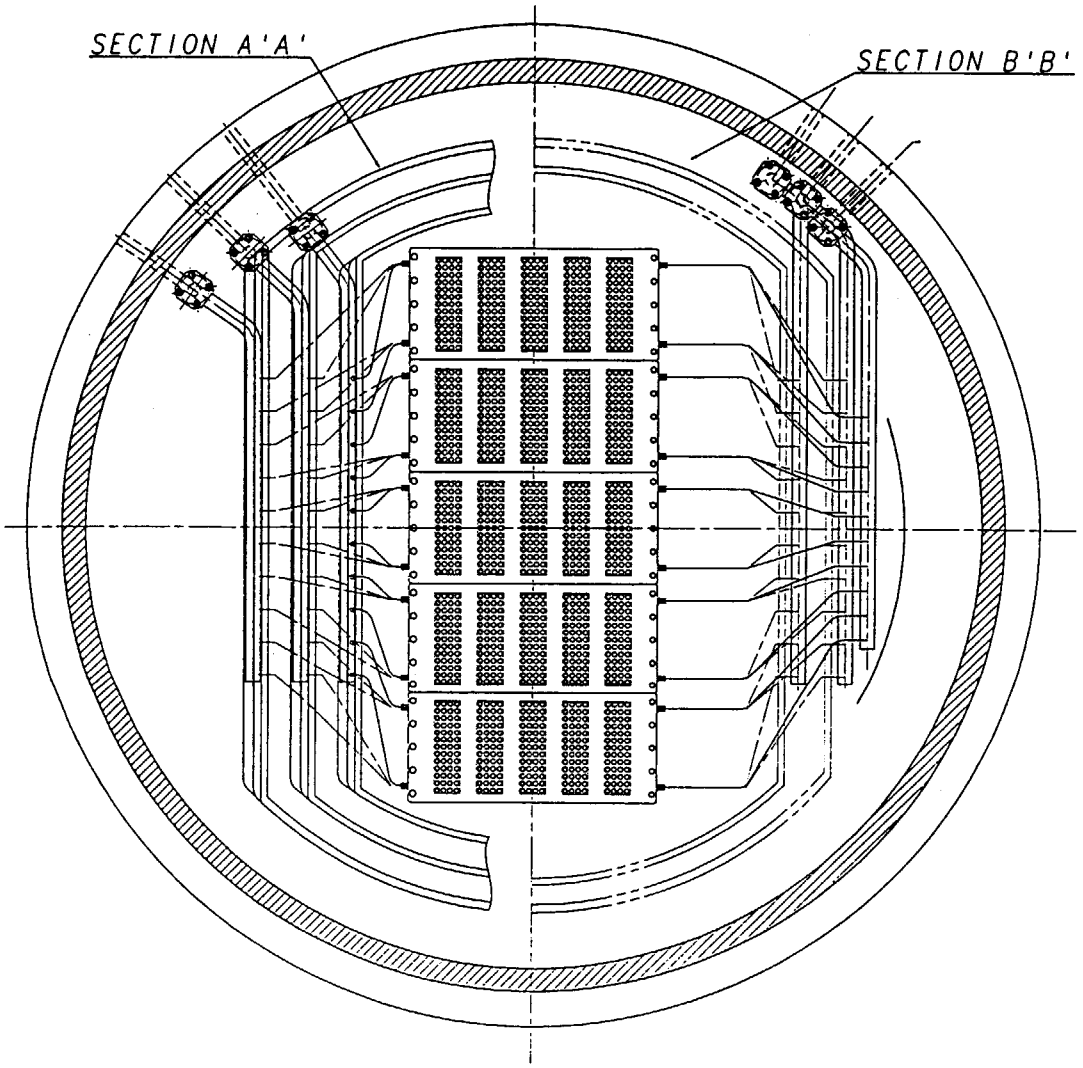

Figure 2.1 Cross sectional view of the ITER accelerator. An acceleration grid consists of five segments, whose dimensions are 756 mm long and 337.5 mm wide.

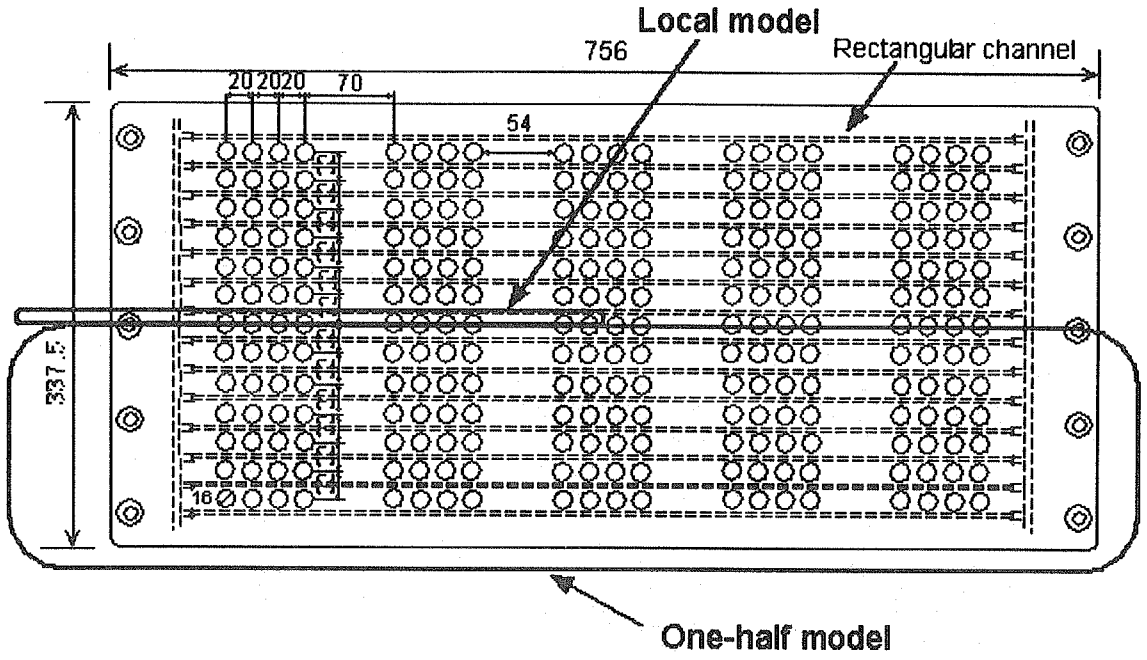

Figure 2.2 A single segment of the ITER acceleration grid. The segment consists of five sub-segments, which have 52 apertures. Two types of computational models were adopted to calculate thermo-mechanical characteristics.

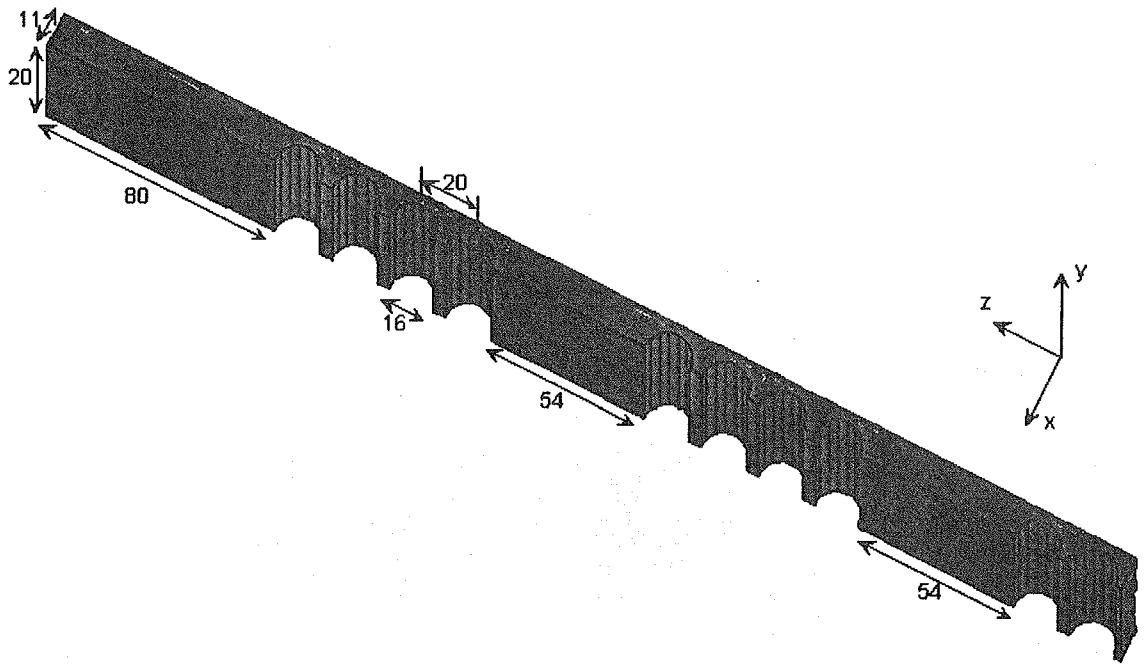

Figure 3.1 Local model from a front view. Precise temperature and stress distributions of the acceleration grid were calculated.

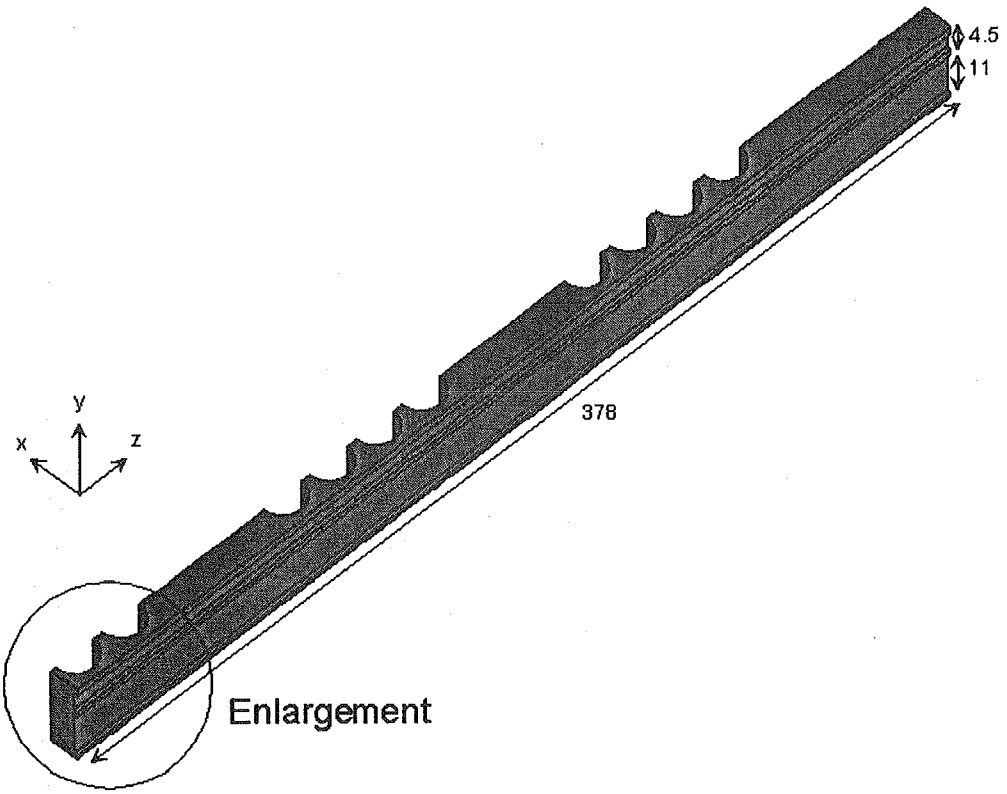

Figure 3.2 Local model from an end view. Precise temperature and stress distributions of the acceleration grid were calculated.

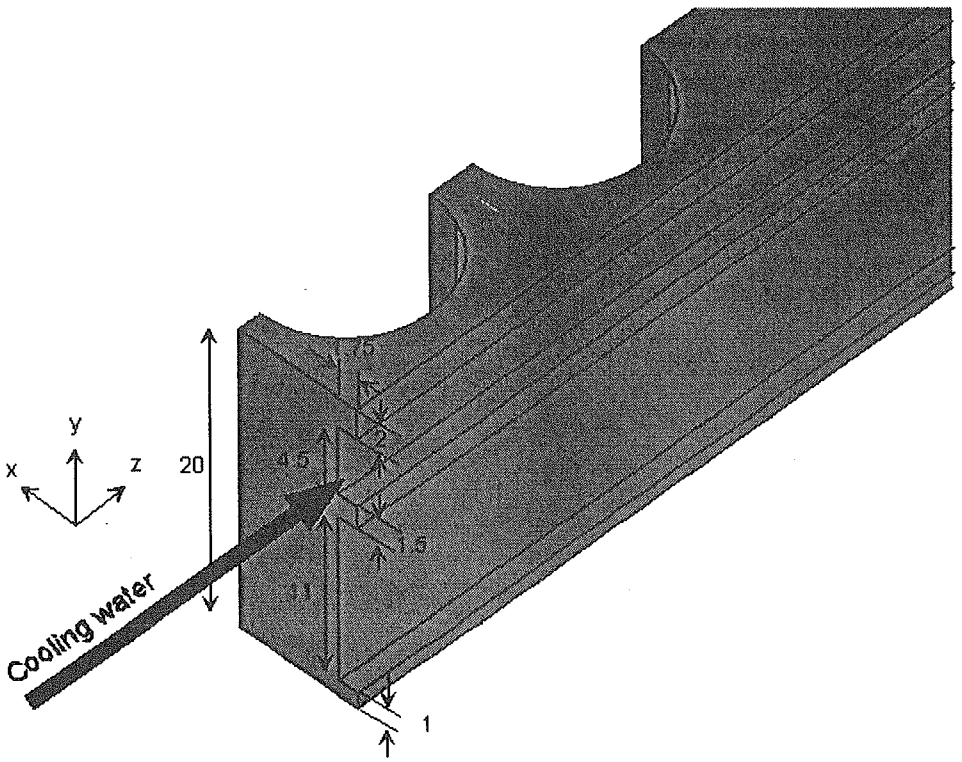

Figure 3.3 A close-up view of the local model.

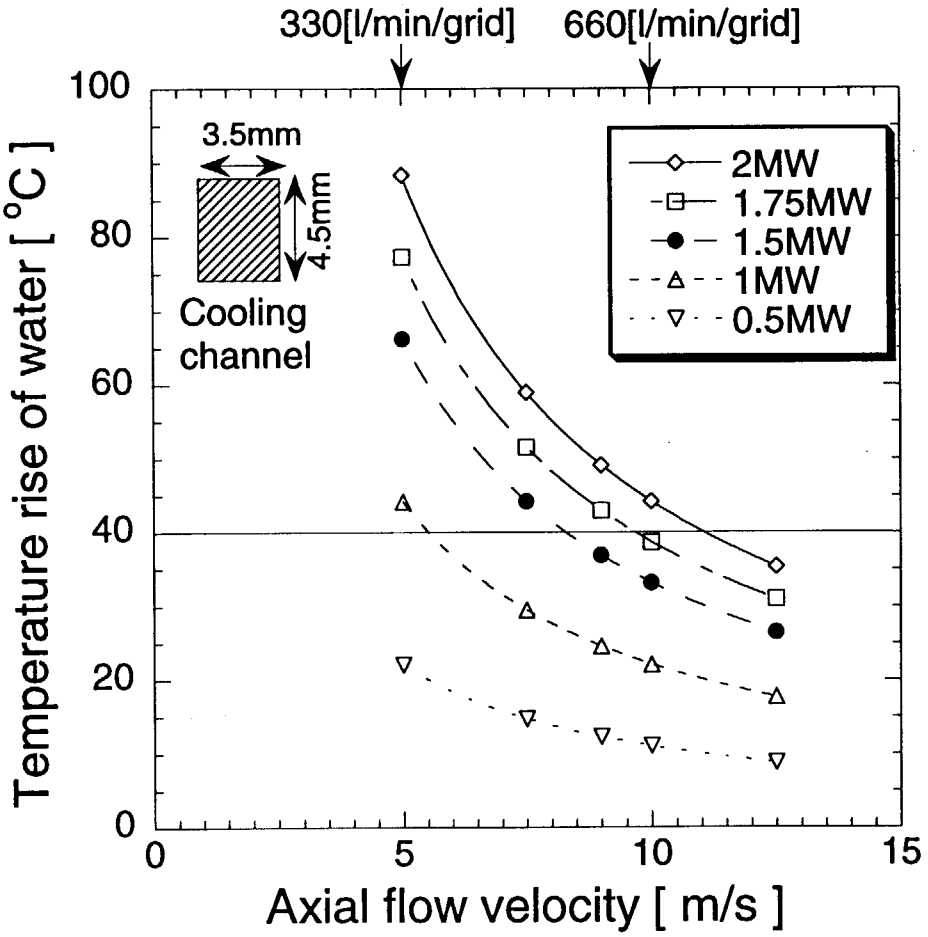

Figure 3.4 Temperature rise of cooling water as a function of axial flow velocity. Dimensions of cooling channel are 4.5 mm high and 3.5 mm wide.

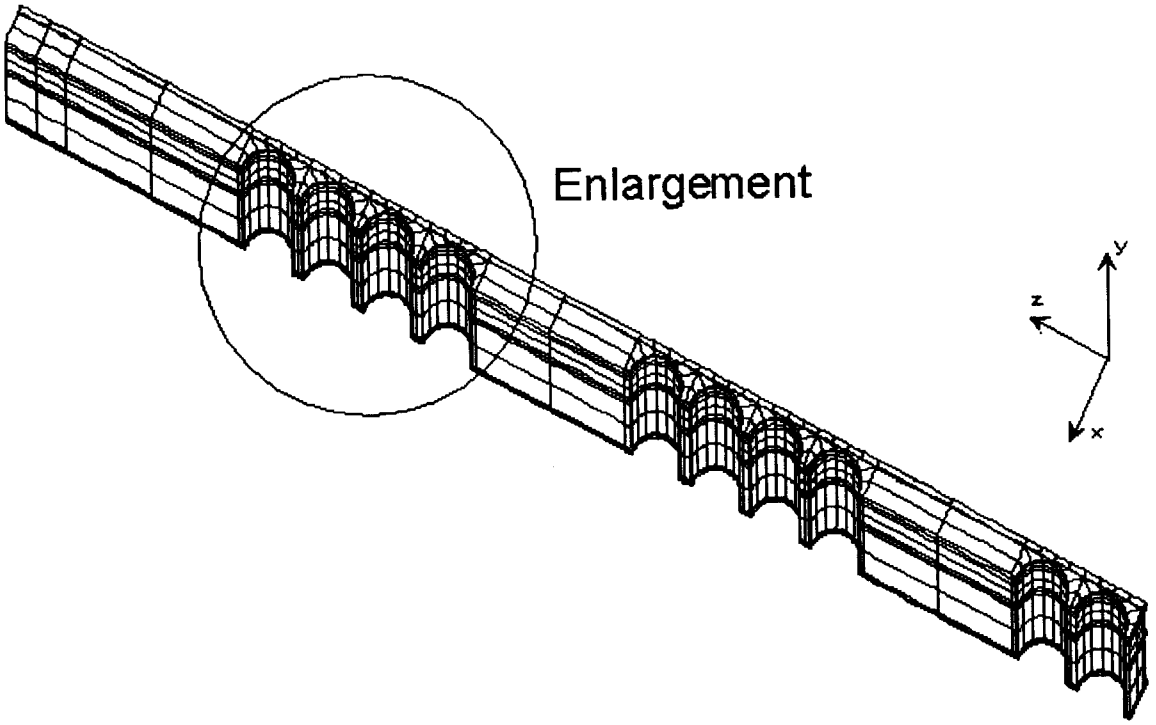

Figure 3.5 Finite element mesh of the local model from a front view.

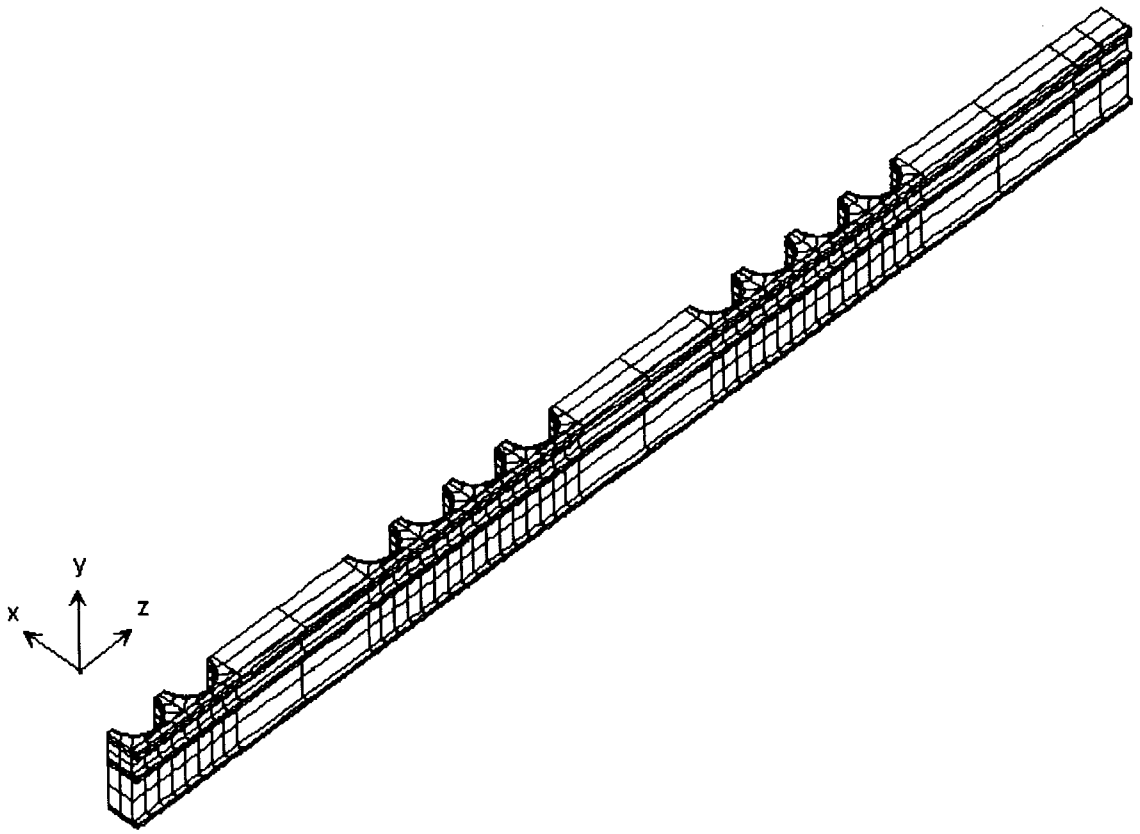

Figure 3.6 Finite element mesh of the local model from an end view.

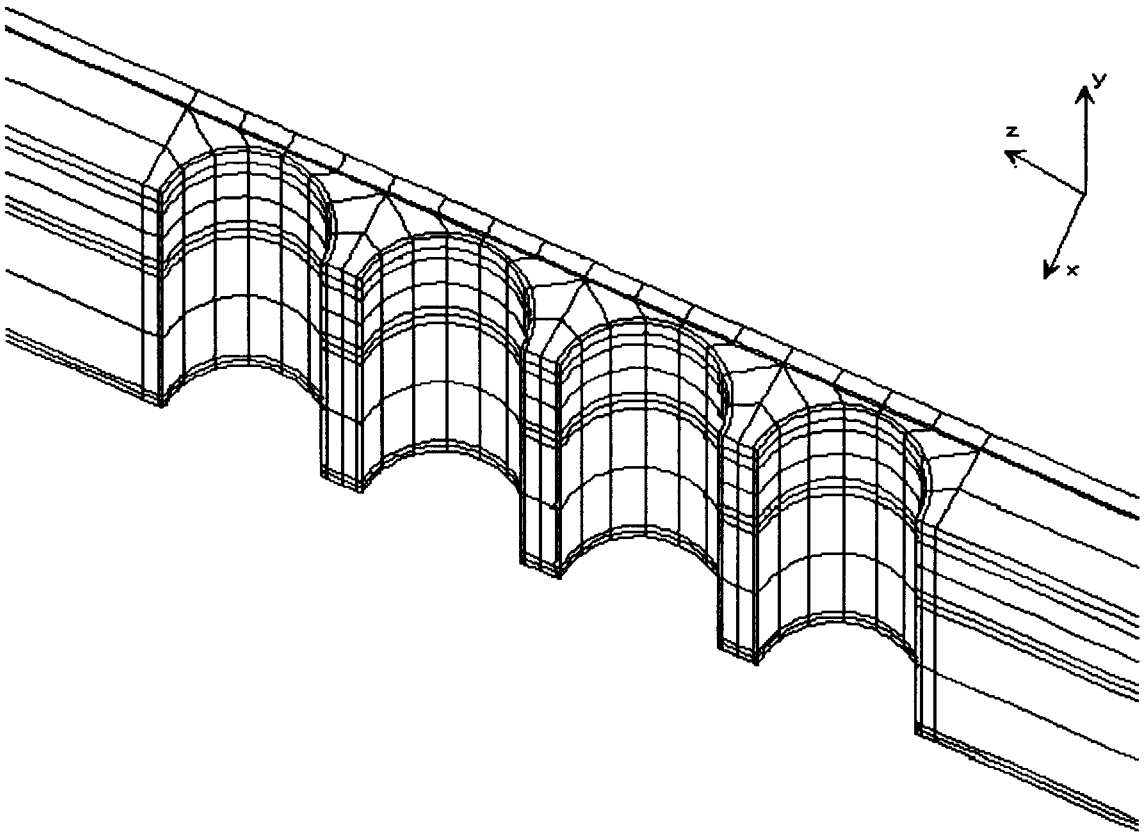

Figure 3.7 A close-up view of the finite element mesh of the local model.

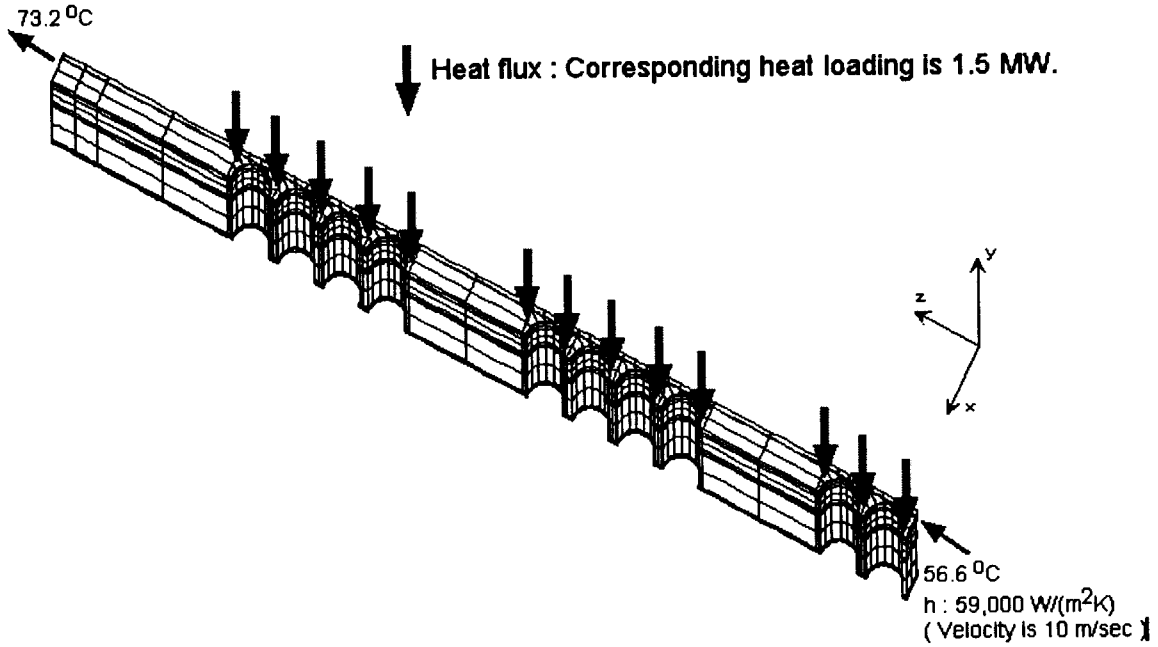

Figure 3.8 Boundary conditions for the thermal analysis. Heat flux was assumed to be injected around apertures.

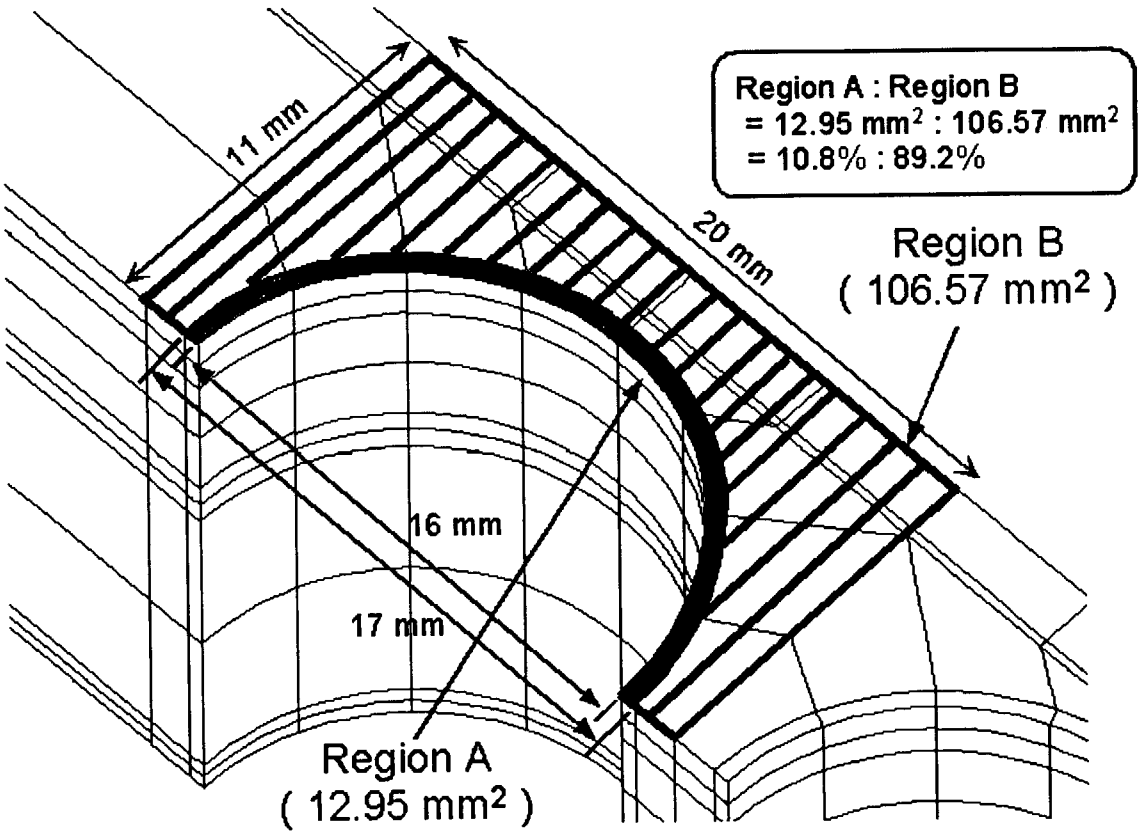

Figure 3.9 Heat loading was distributed on both region A and region B.

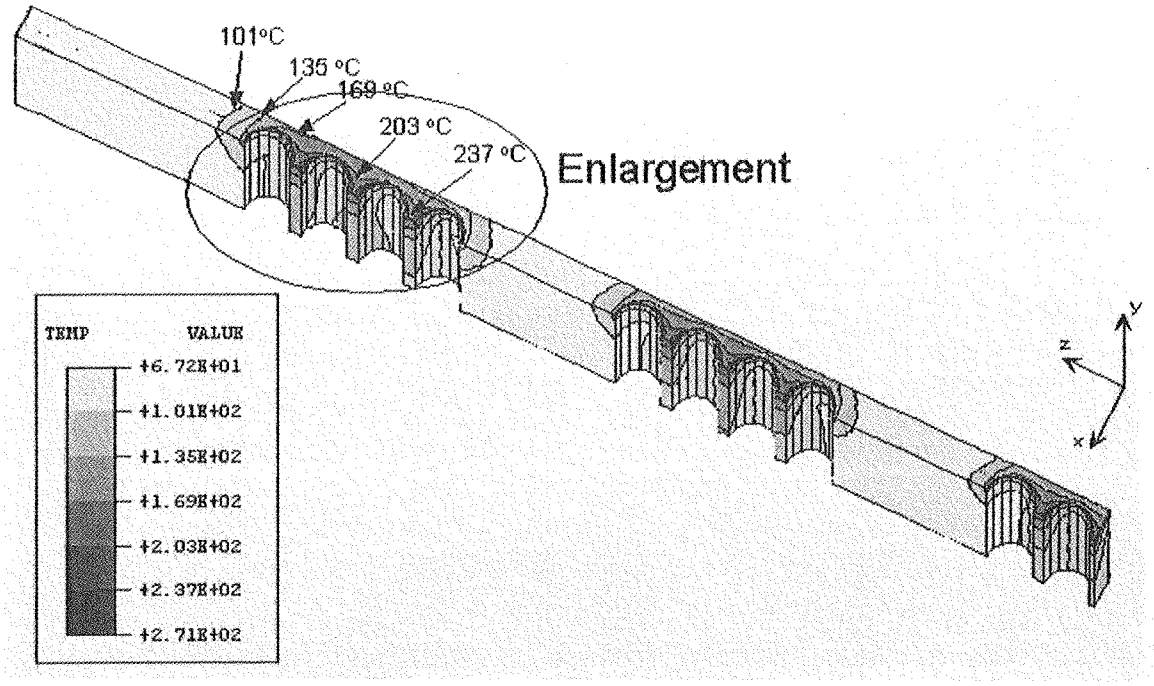

Figure 3.10 Temperature distribution from a front view for the heat loading of 1.5 MW. The heat flux distribution of case 1 was assumed.

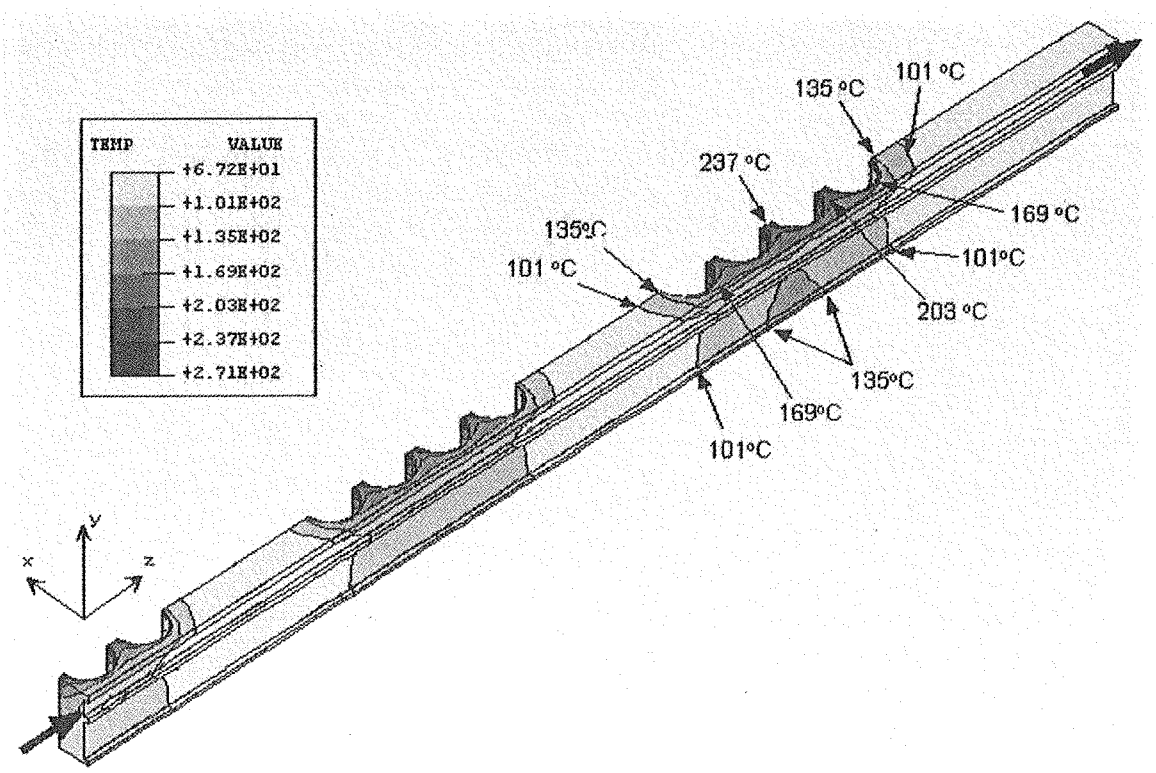

Figure 3.11 Temperature distribution from an end view for the heat loading of 1.5 MW. The heat flux distribution of case 1 was assumed.

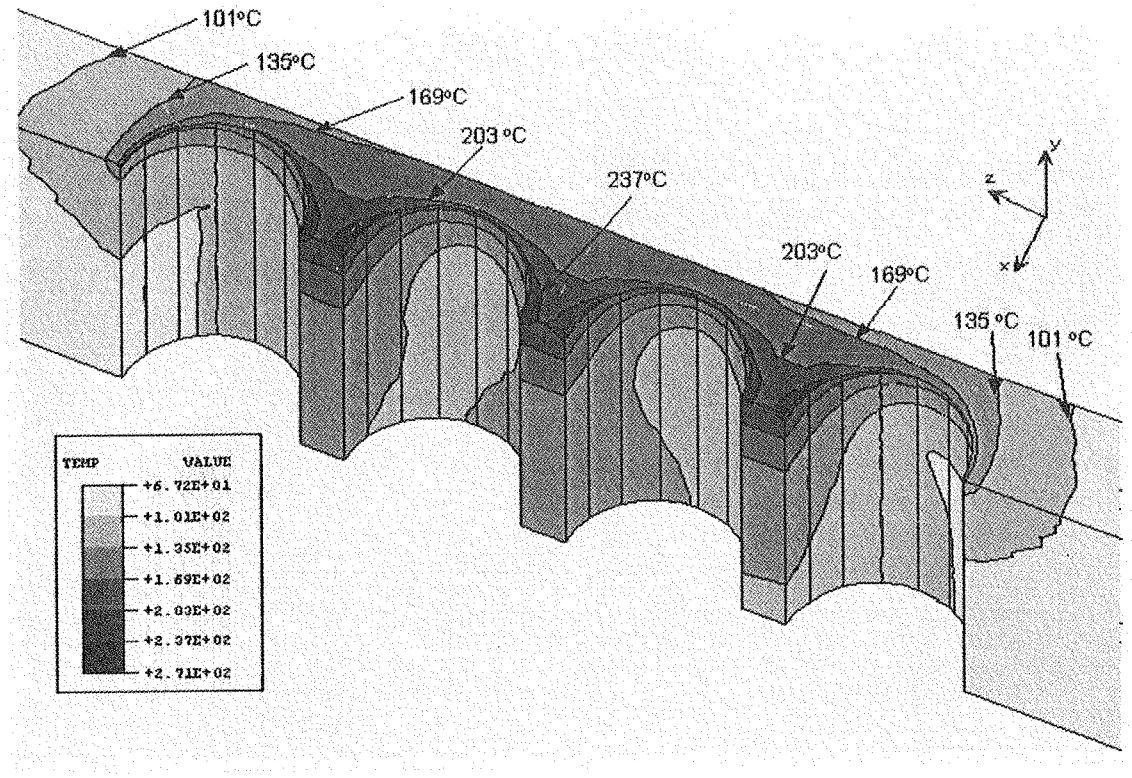

Figure 3.12 A close-up view of temperature distribution for the heat loading of 1.5 MW. The heat flux distribution of case 1 was assumed.

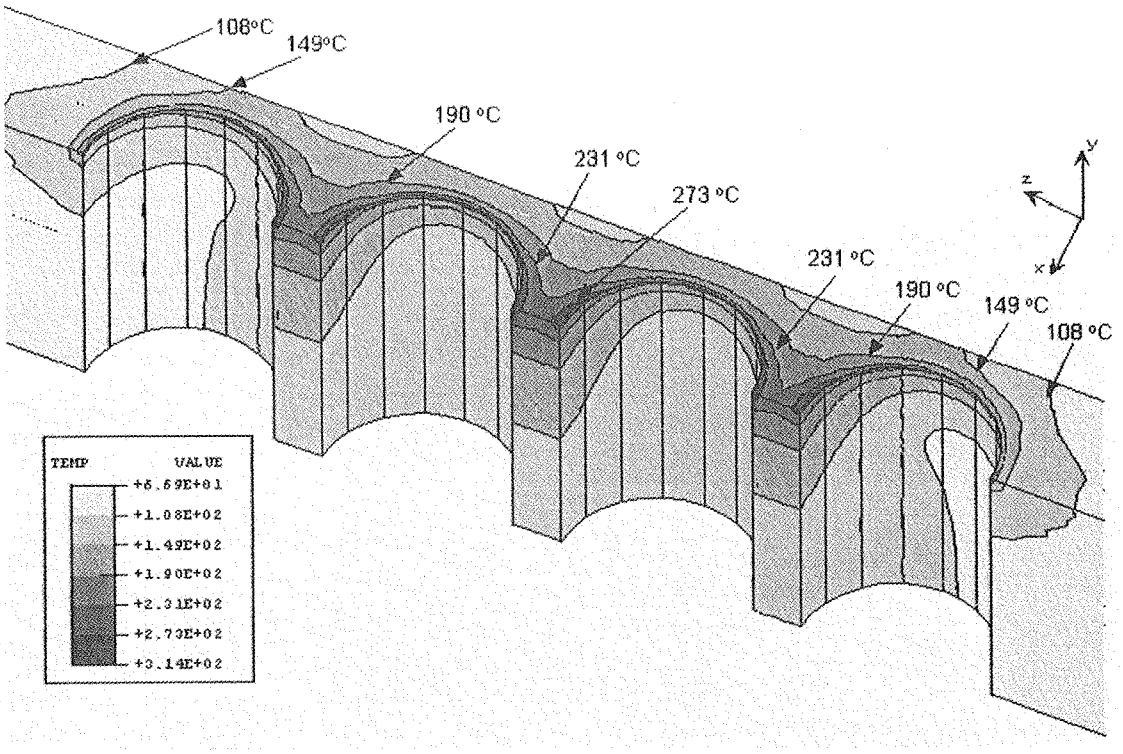

Figure 3.13 A close-up view of temperature distribution for the heat loading of 1.5 MW. The heat flux distribution of case 2 was assumed.

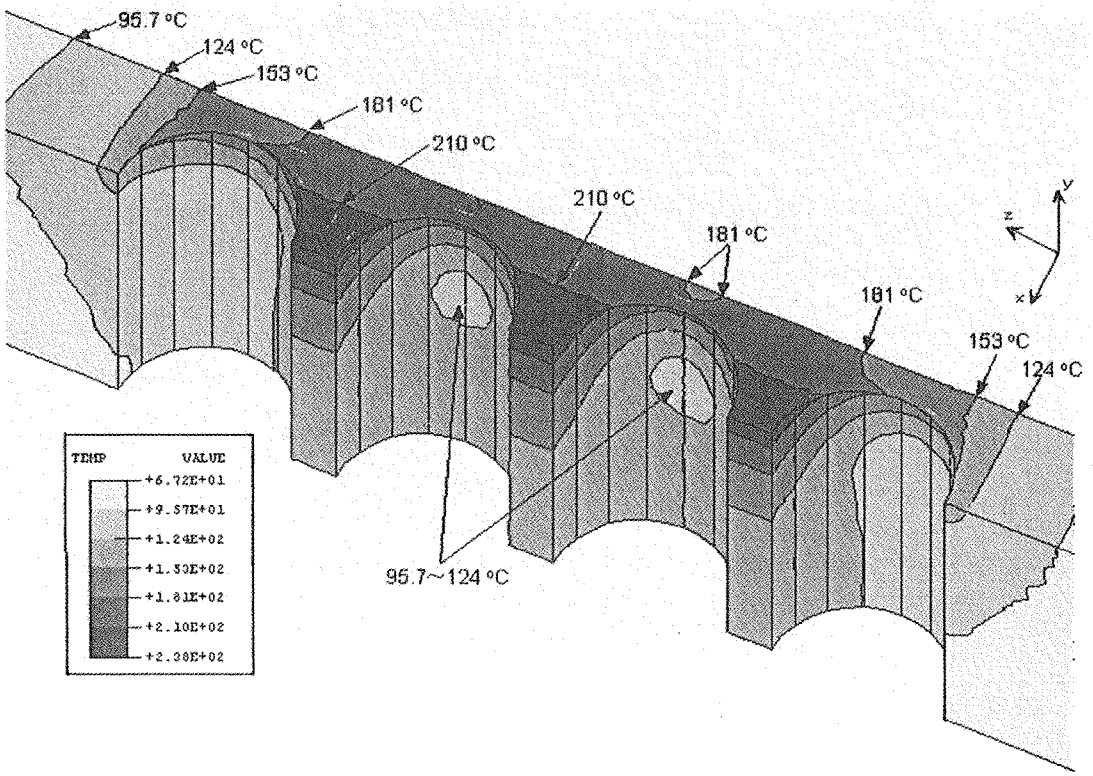

Figure 3.14 A close-up view of temperature distribution for the heat loading of 1.5 MW. The heat flux distribution of case 3 was assumed.

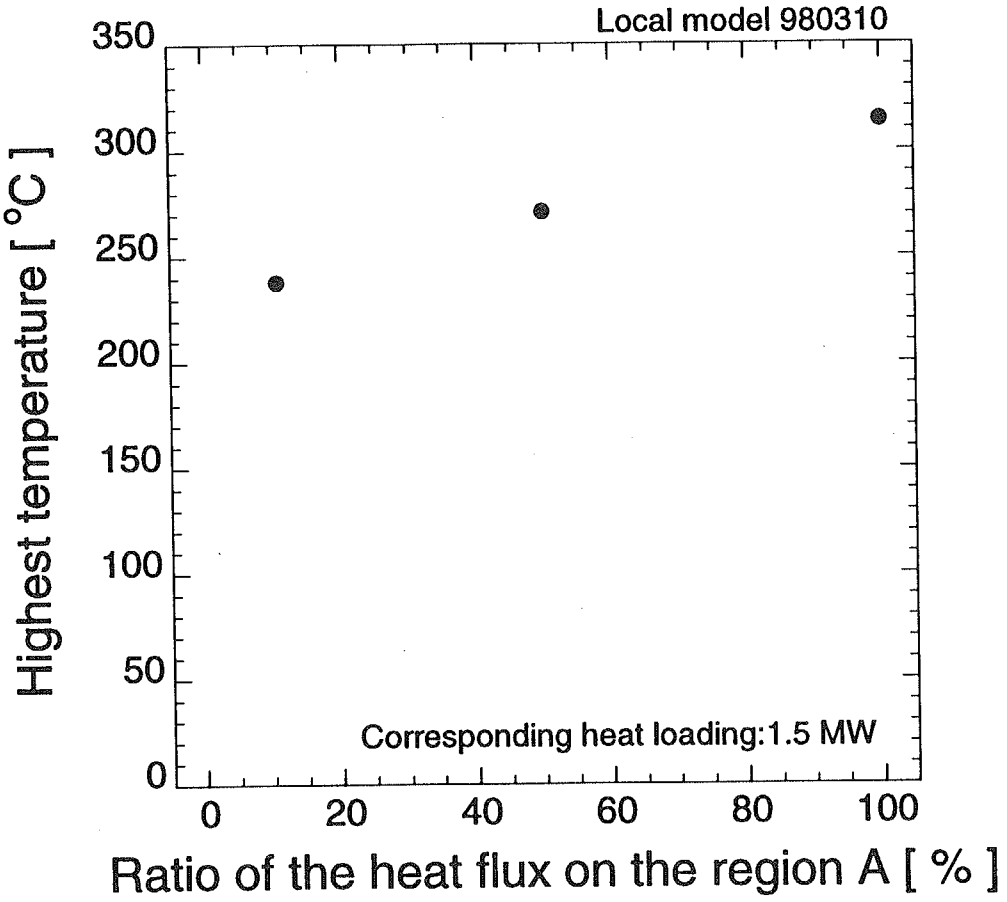

Figure 3.15 Highest temperature as a function of the ratio of the heat flux on the region A. Heat loading was assumed to be 1.5 MW.

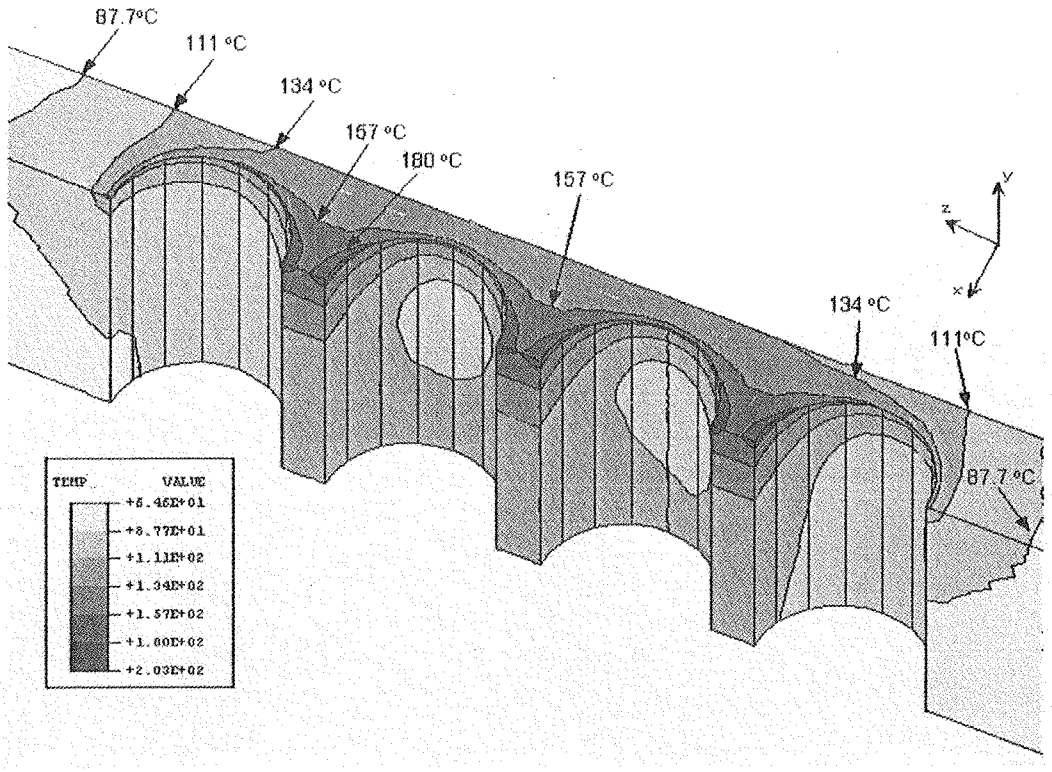

Figure 3.16 A close-up view of temperature distribution for the heat loading of 1 MW. The heat flux distribution of case 1 was assumed.

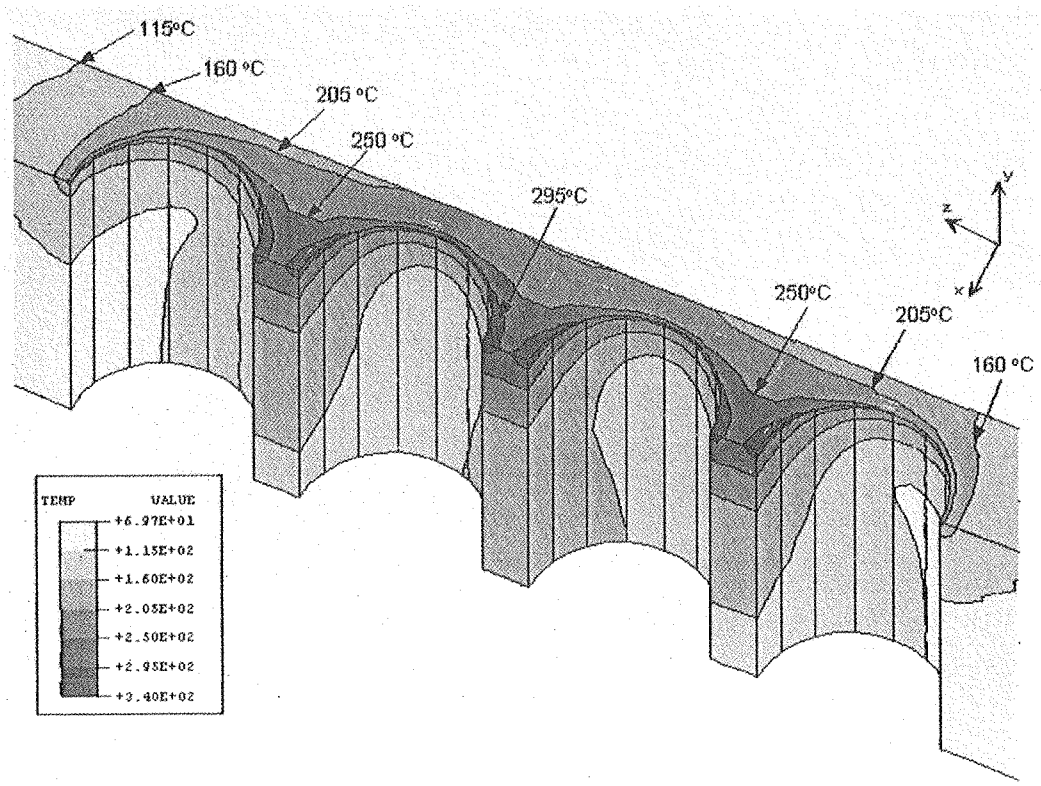

Figure 3.17 A close-up view of temperature distribution for the heat loading of 2 MW. The heat flux distribution of case 1 was assumed.

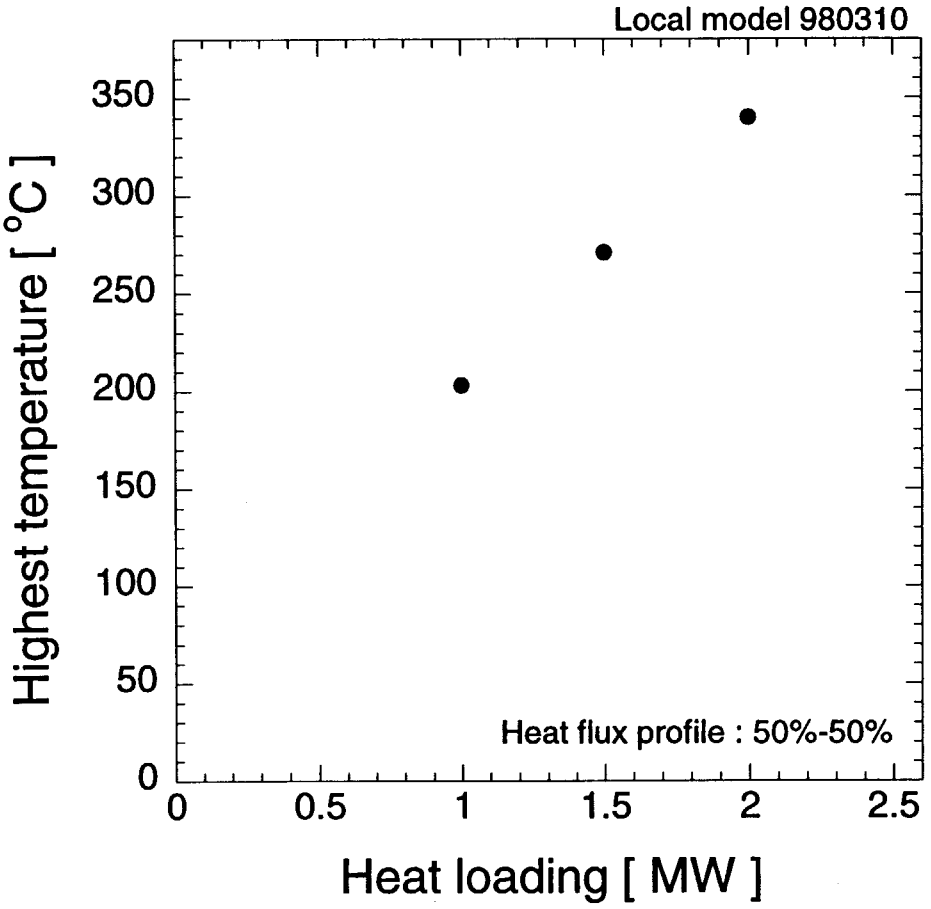

Figure 3.18 Highest temperature versus heat loading. The heat flux distribution of case 1 was assumed.

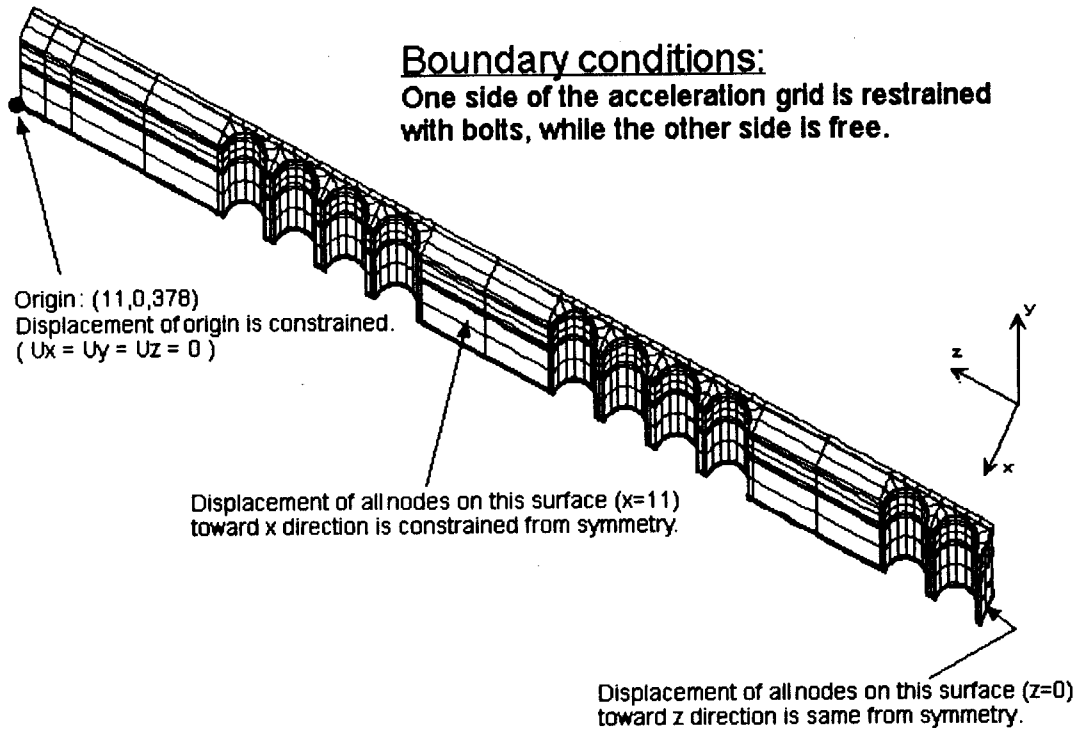

Figure 3.19 Boundary conditions for the elastic thermal stress analysis. The displacement of origin was constrained (Ux = Uy = Uz = 0).

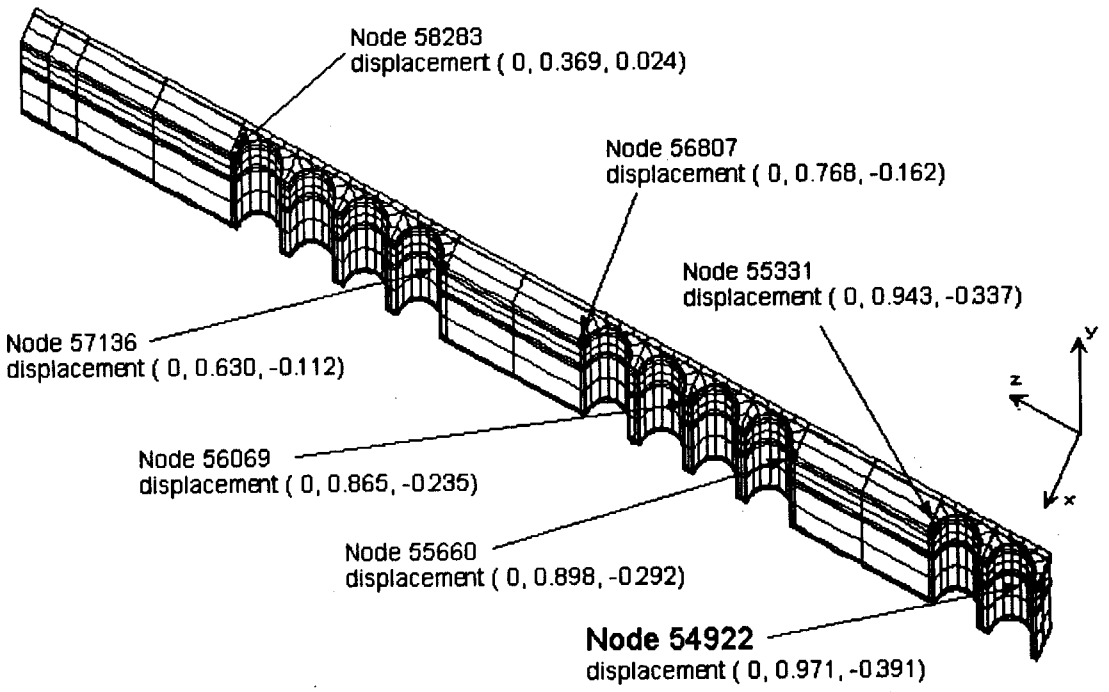

Figure 3.20 Node points and their displacement for the heat loading of 1.5 MW. The heat flux distribution of case 1 was assumed.

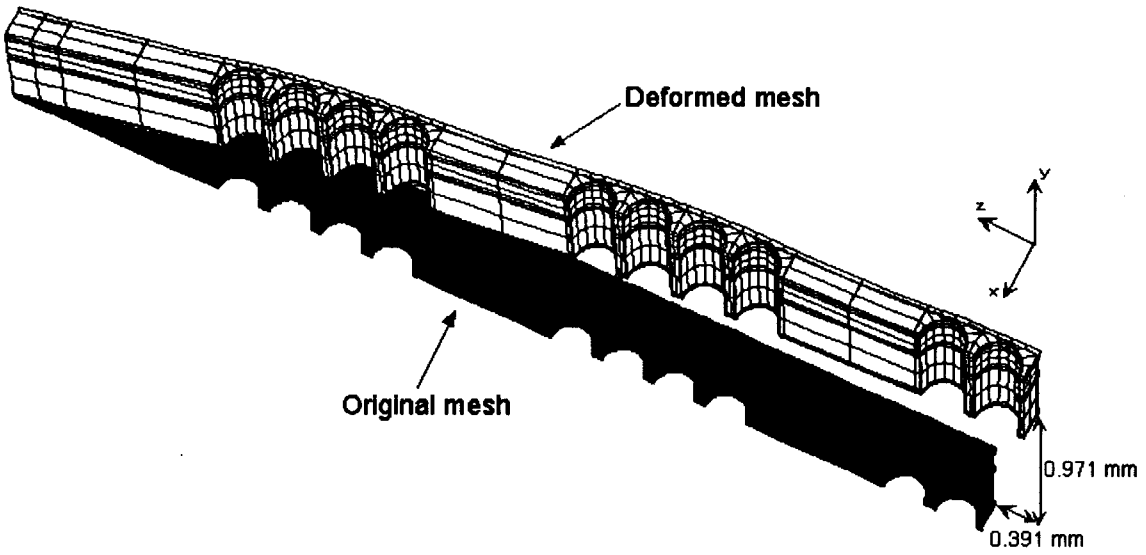

Figure 3.21 Thermal deformation, enlarged by a factor of 40, for the heat loading of 1.5 MW. The heat flux distribution of case 1 was assumed.

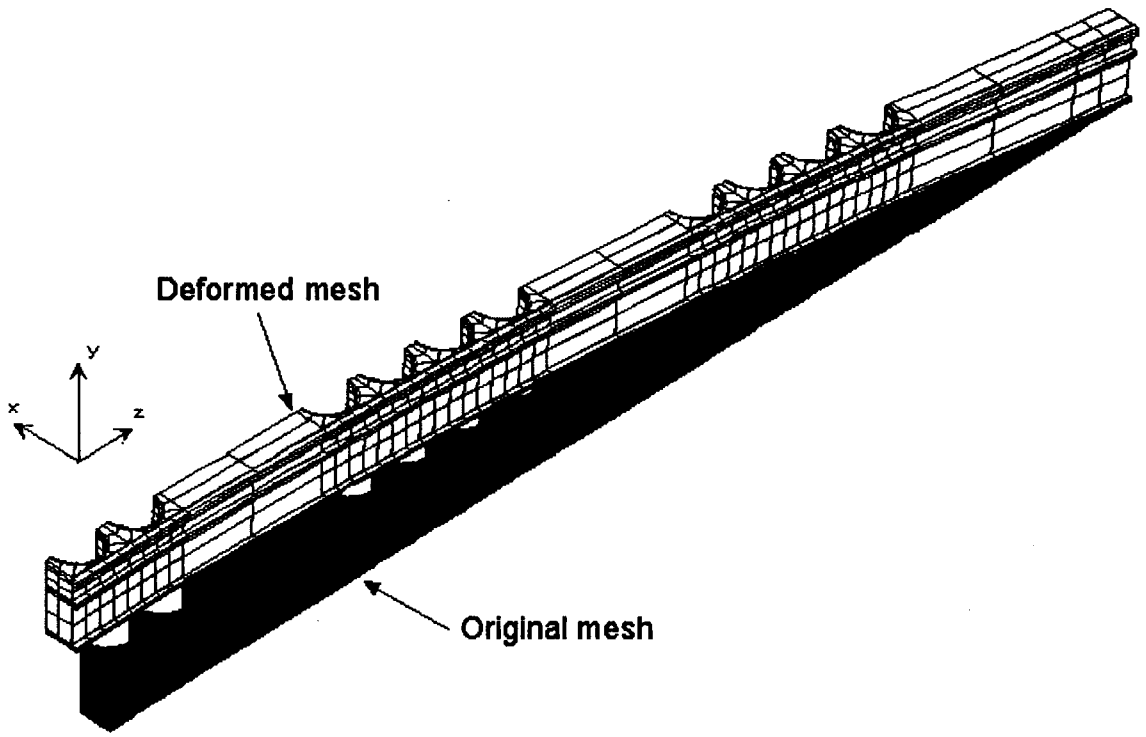

Figure 3.22 Thermal deformation, enlarged by a factor of 30, from an end view.

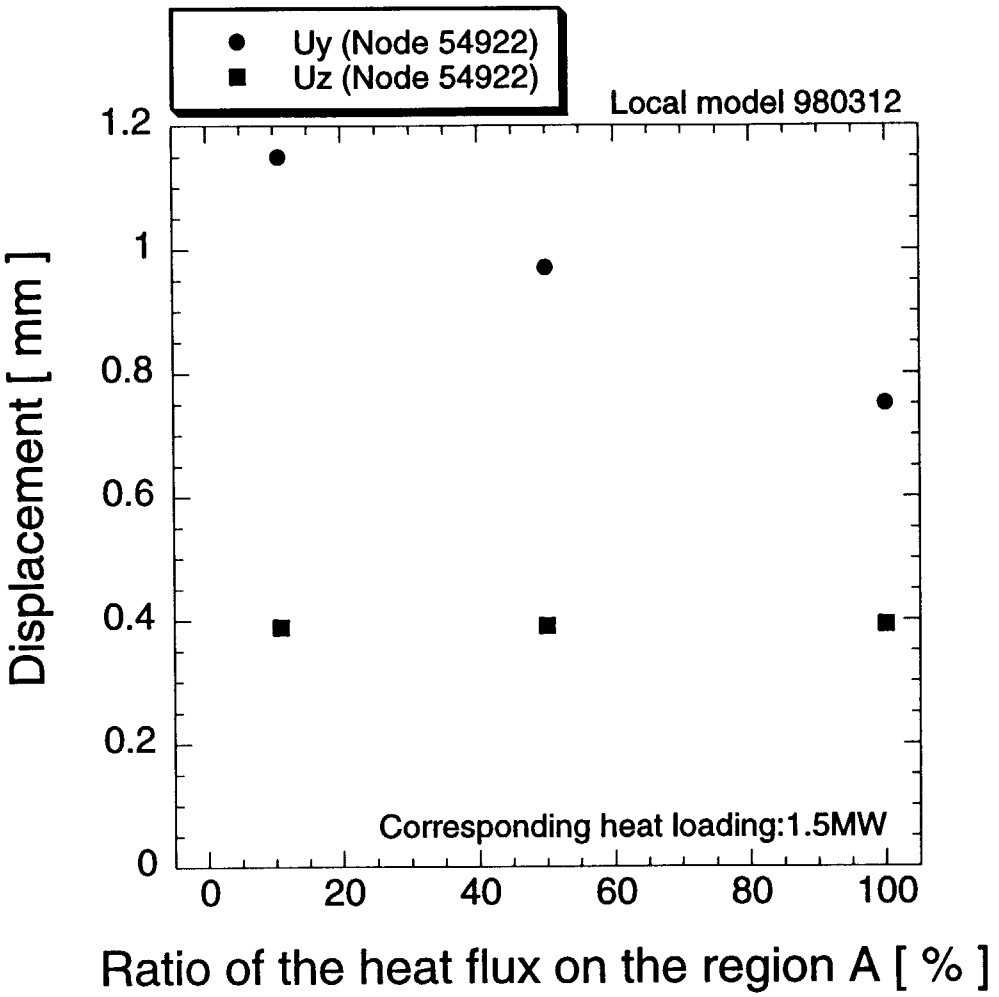

Figure 3.23 Displacement of central part as a function of the ratio of the heat flux on the region A. Heat loading was assumed to be 1.5 MW.

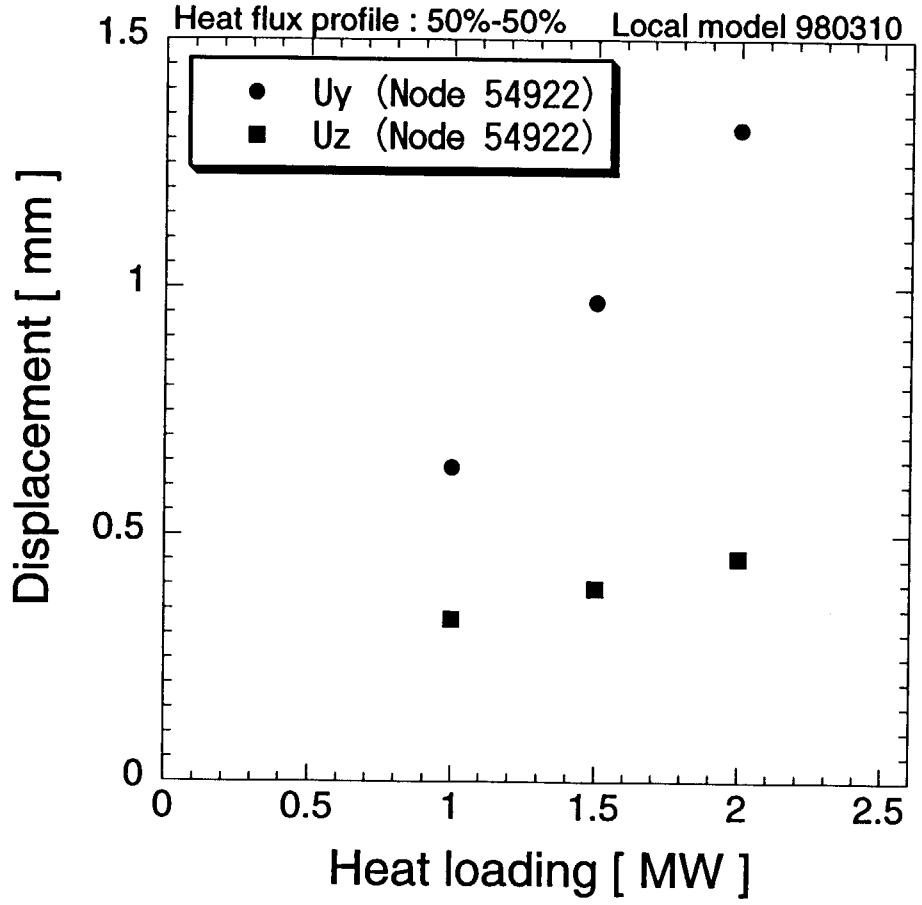

Figure 3.24 Displacement of central part as a function of heat loading. The heat flux distribution of case 1 was assumed.

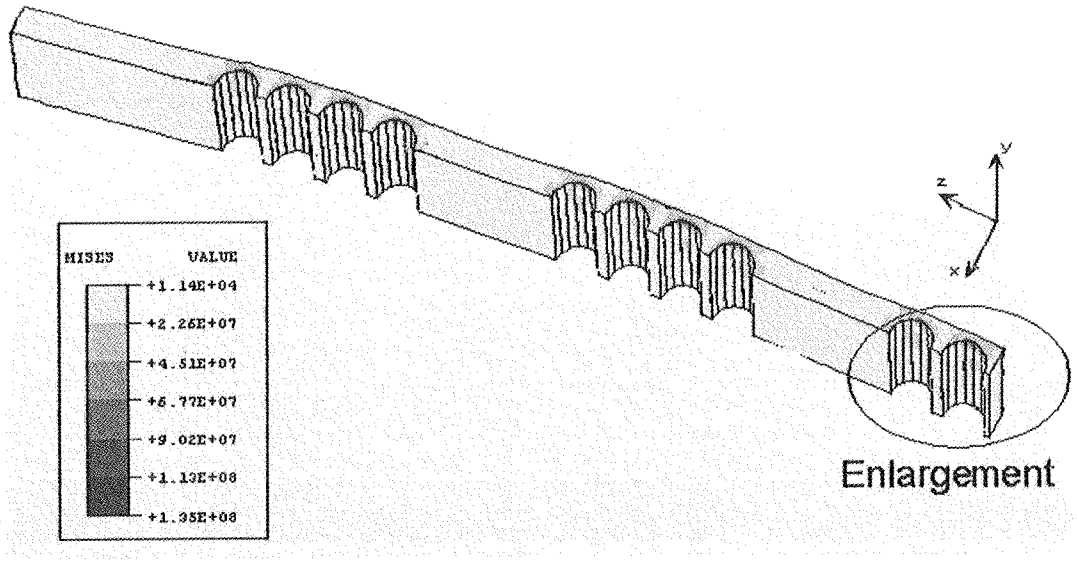

Figure 3.25 Von Mises equivalent stress distribution from a front view for the heat loading of 1.5 MW. The heat flux distribution of case 1 was assumed.

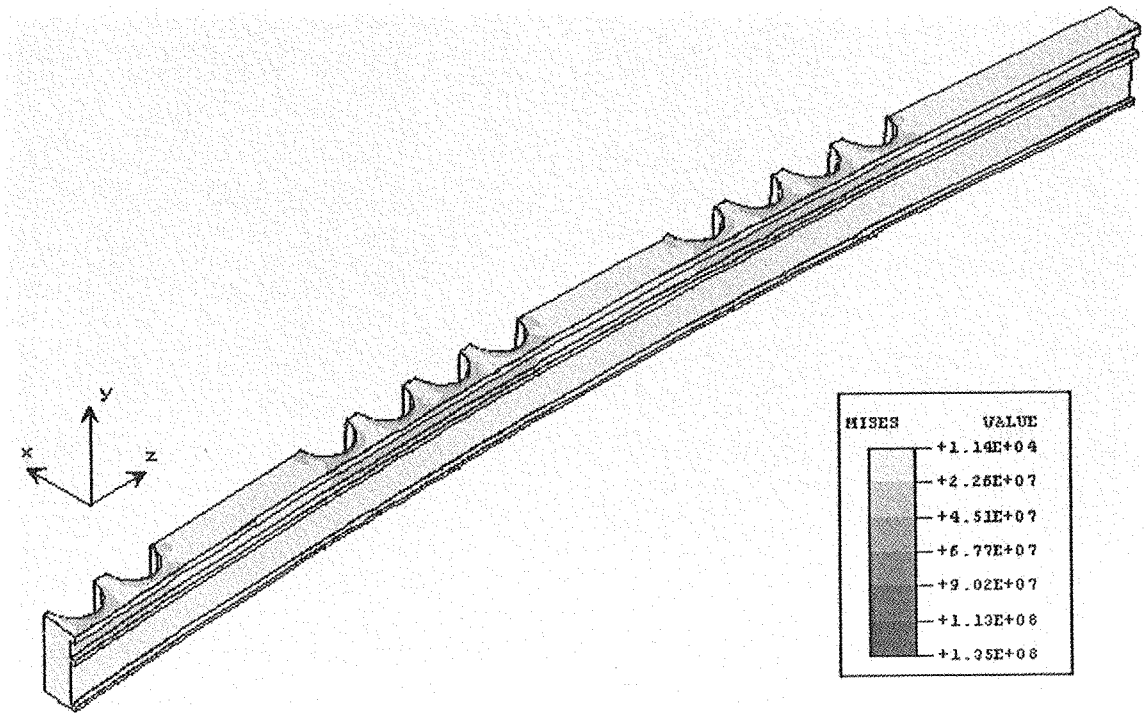

Figure 3.26 Von Mises equivalent stress distribution from an end view for the heat loading of 1.5 MW. The heat flux distribution of case 1 was assumed.

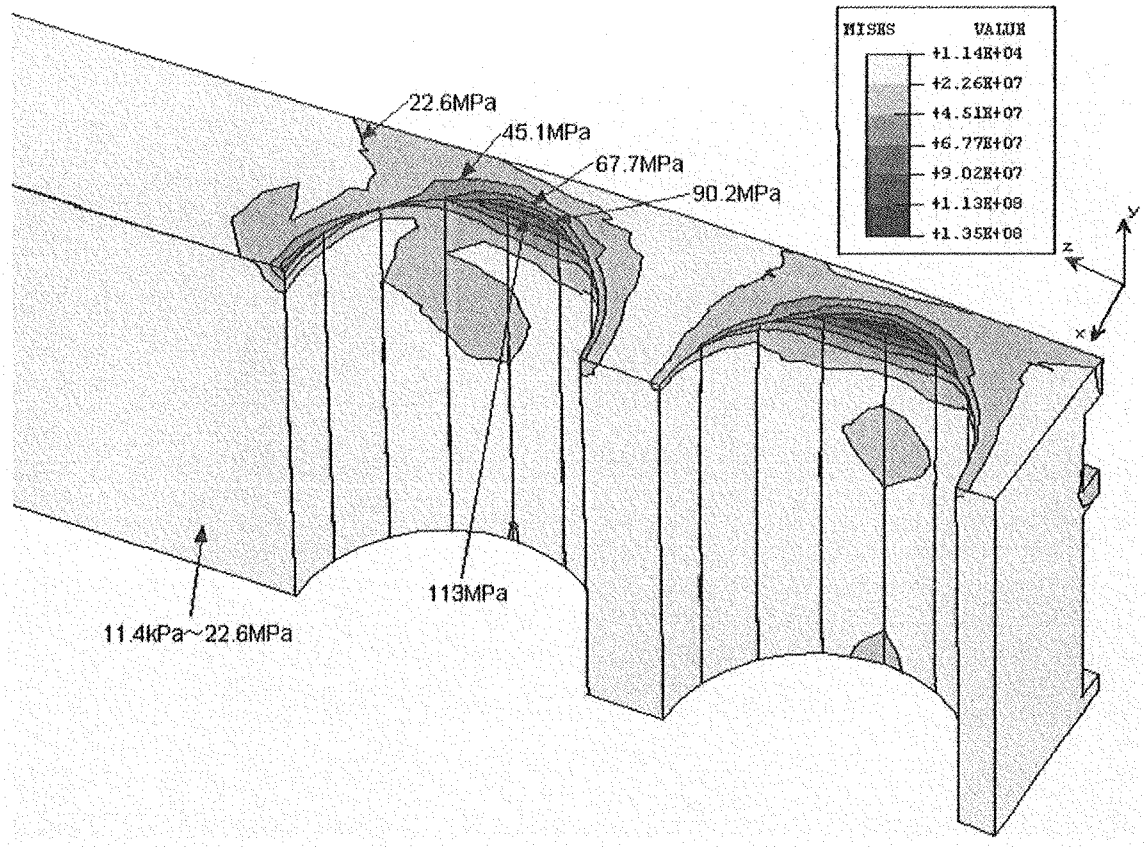

Figure 3.27 A close-up view of von Mises equivalent stress distribution for the heat loading of 1.5 MW. The heat flux distribution of case 1 was assumed.

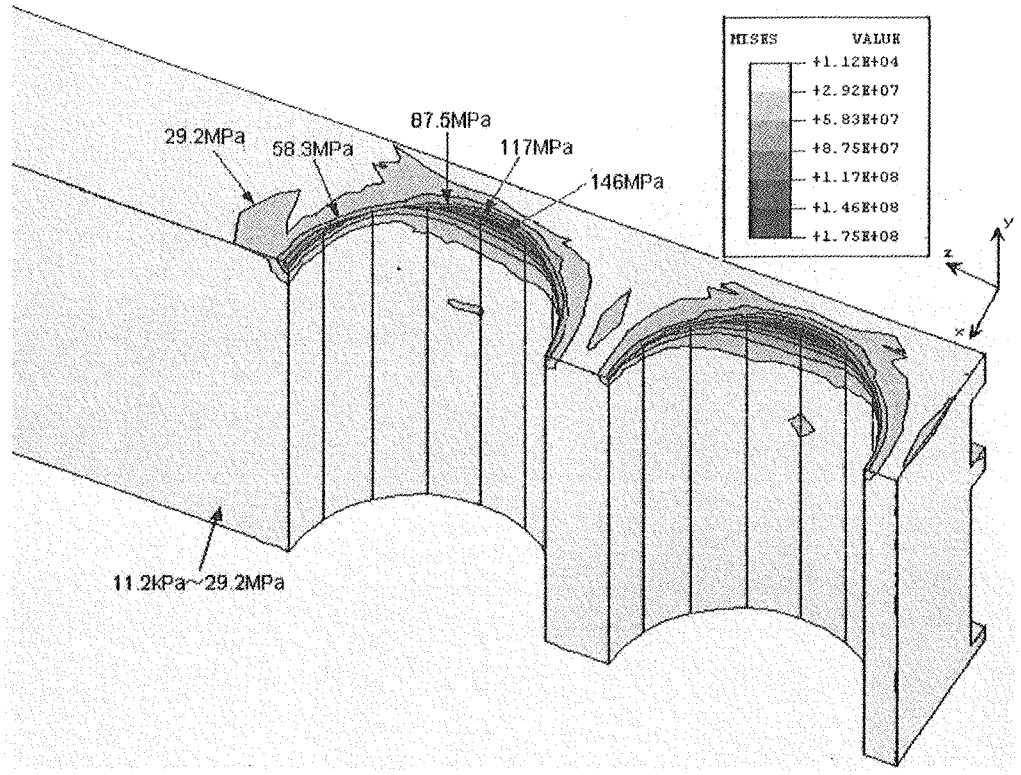

Figure 3.28 A close-up view of von Mises equivalent stress distribution for the heat loading of 1.5 MW. The heat flux distribution of case 2 was assumed.

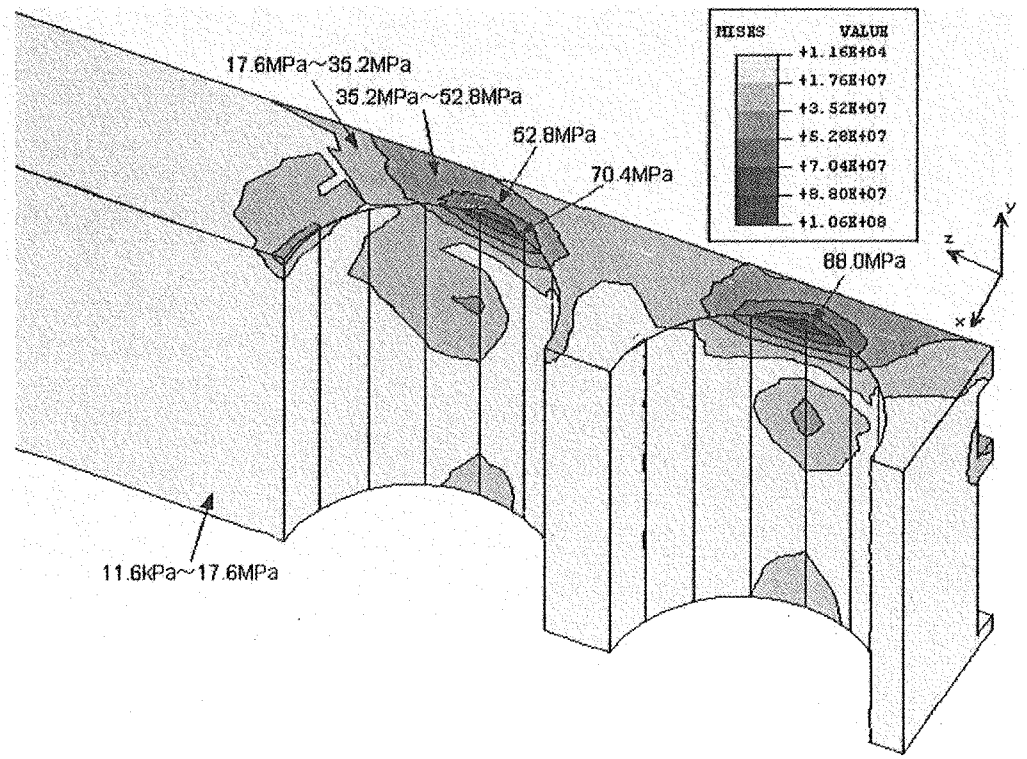

Figure 3.29 A close-up view of von Mises equivalent stress distribution for the heat loading of 1.5 MW. The heat flux distribution of case 3 was assumed.

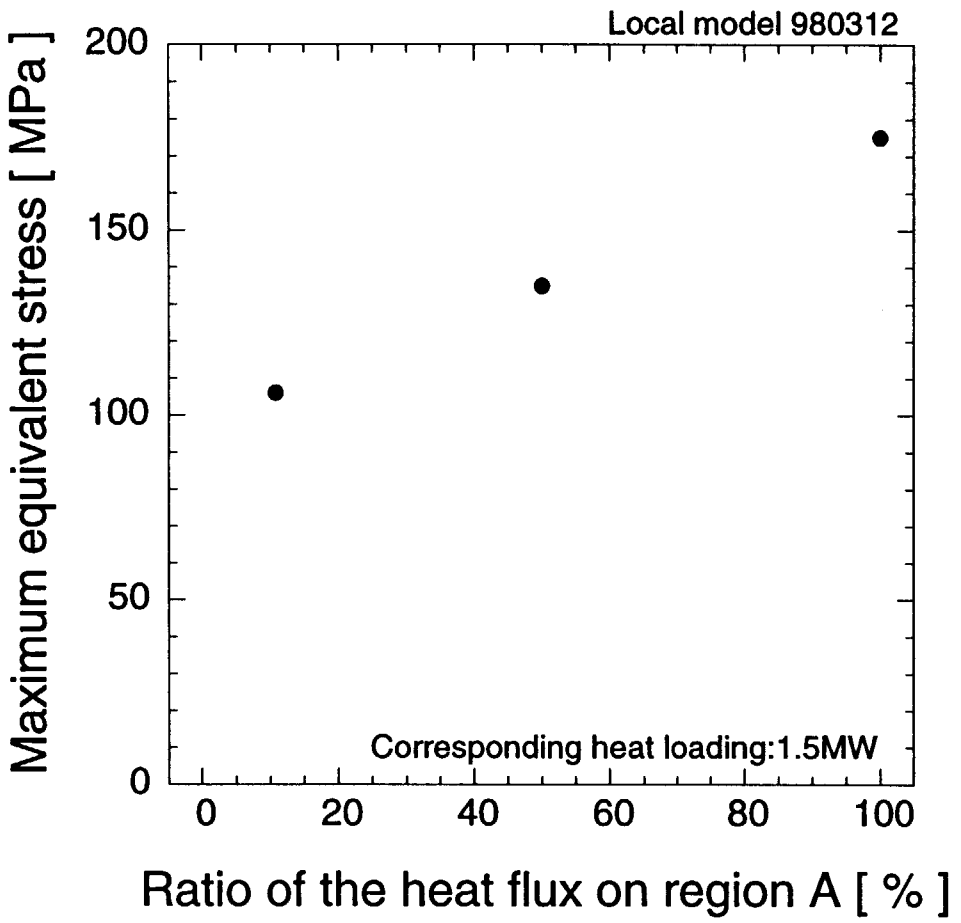

Figure 3.30 Maximum von Mises equivalent stress as a function of the ratio of the heat flux on the region A. Heat loading was assumed to be 1.5 MW.

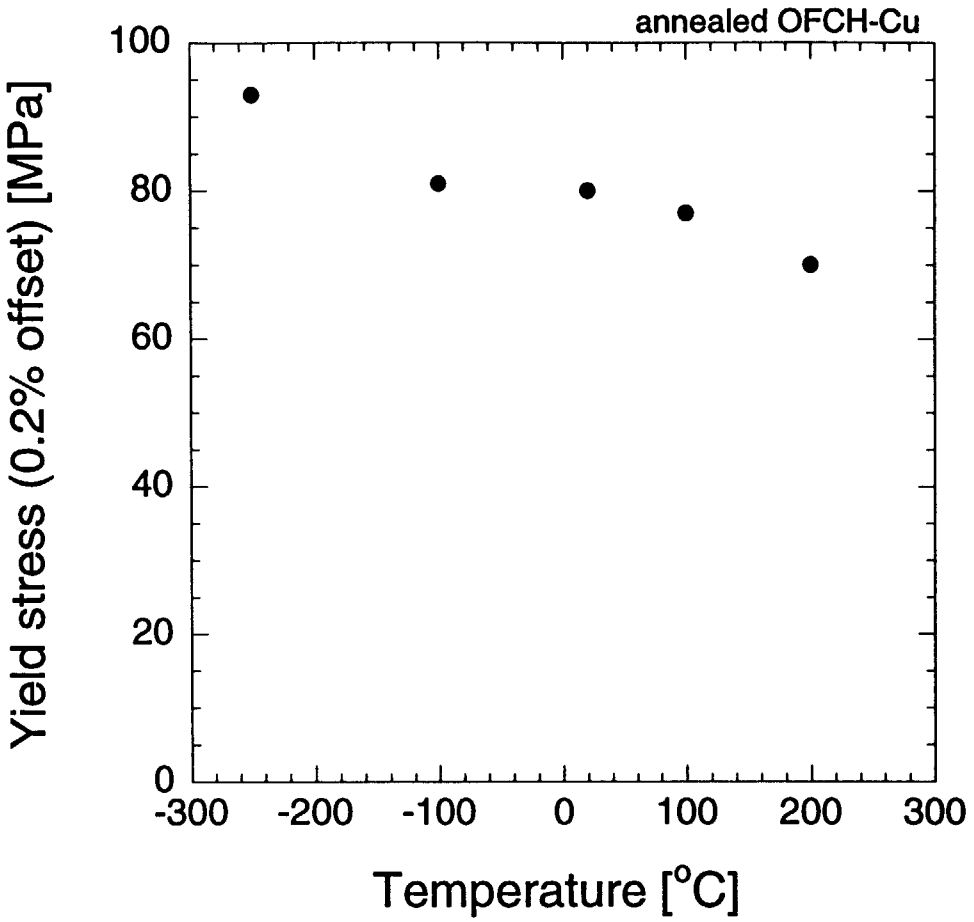

Figure 3.31 Yield stress (0.2% offset) of annealed OFHC-Cu as a function of temperature. (From reference 8)

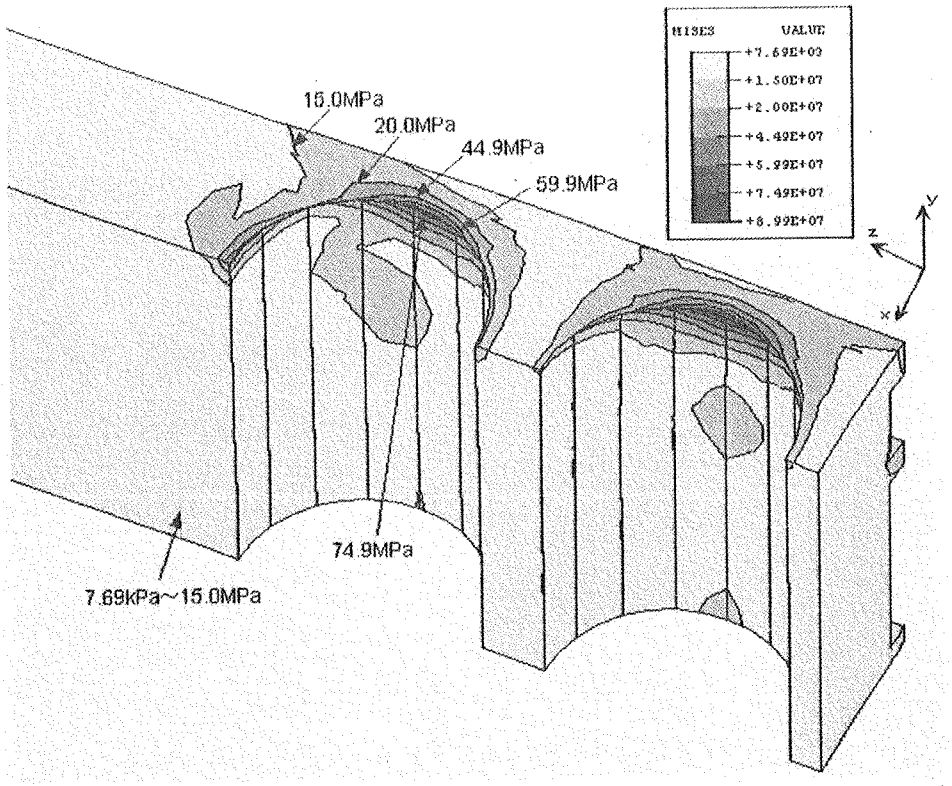

Figure 3.32 A close-up view of von Mises equivalent stress distribution for the heat loading of 1 MW. The heat flux distribution of case 1 was assumed.

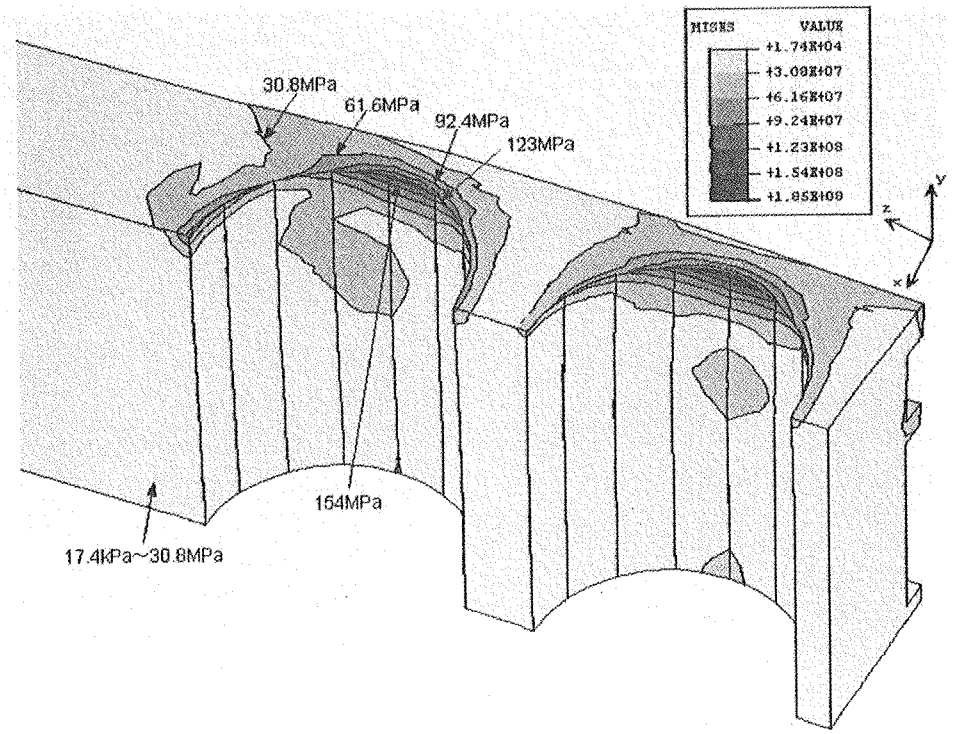

Figure 3.33 A close-up view of von Mises equivalent stress distribution for the heat loading of 2 MW. The heat flux distribution of case 1 was assumed.

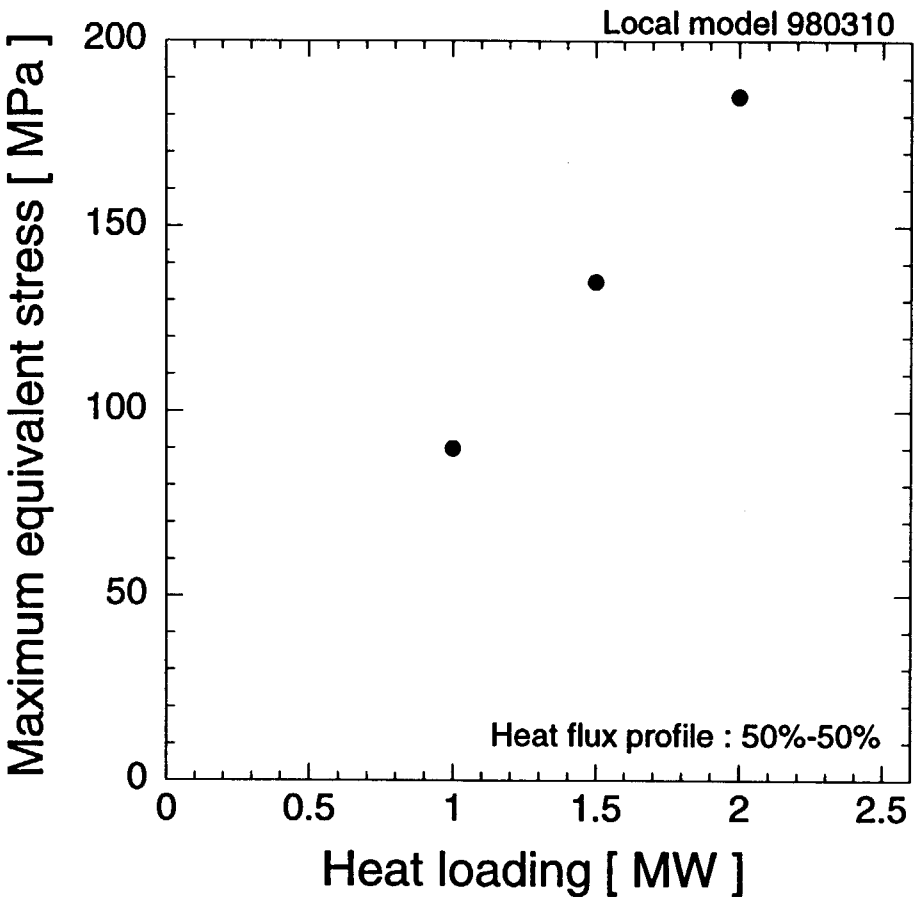

Figure 3.34 Maximum von Mises equivalent stress as a function of heat loading. The heat flux distribution of case 1 was assumed.

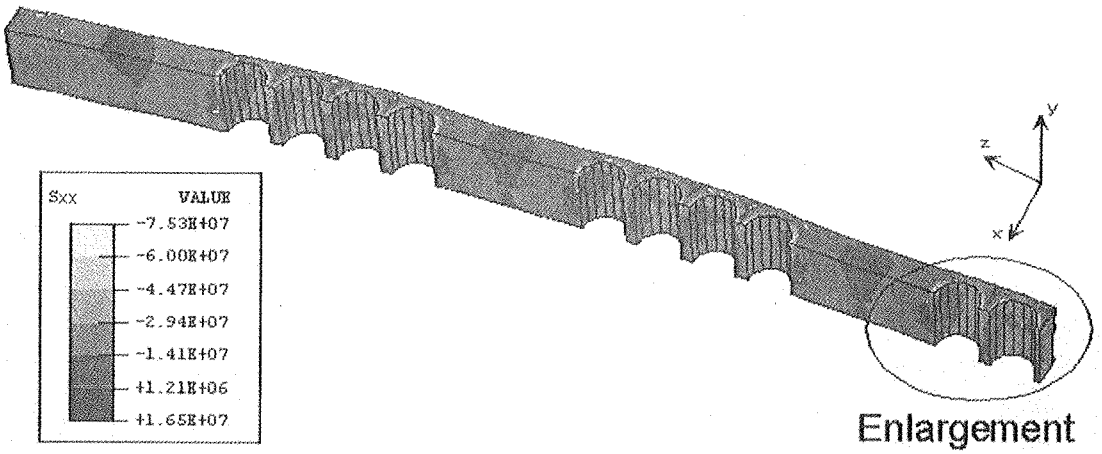

Figure 3.35 Stress component (Sxx) for the heat loading of 1.5 MW. The heat flux distribution of case 1 was assumed.

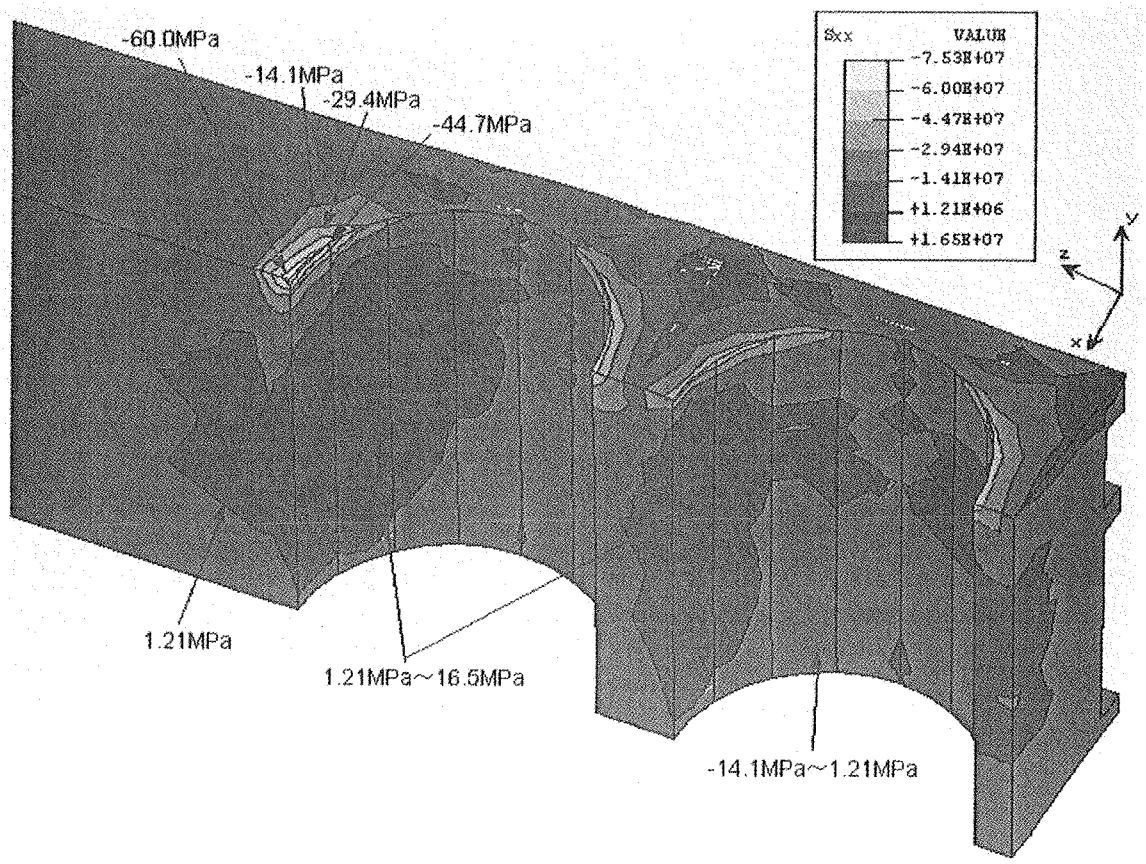

Figure 3.36 A close-up view of stress component (Sxx). The heat flux distribution of case 1 was assumed.

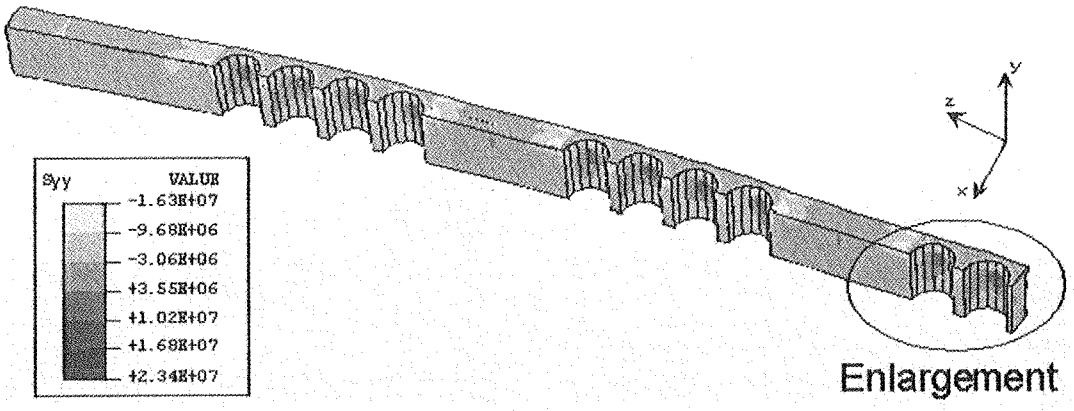

Figure 3.37 Stress component (Syy) for the heat loading of 1.5 MW. The heat flux distribution of case 1 was assumed.

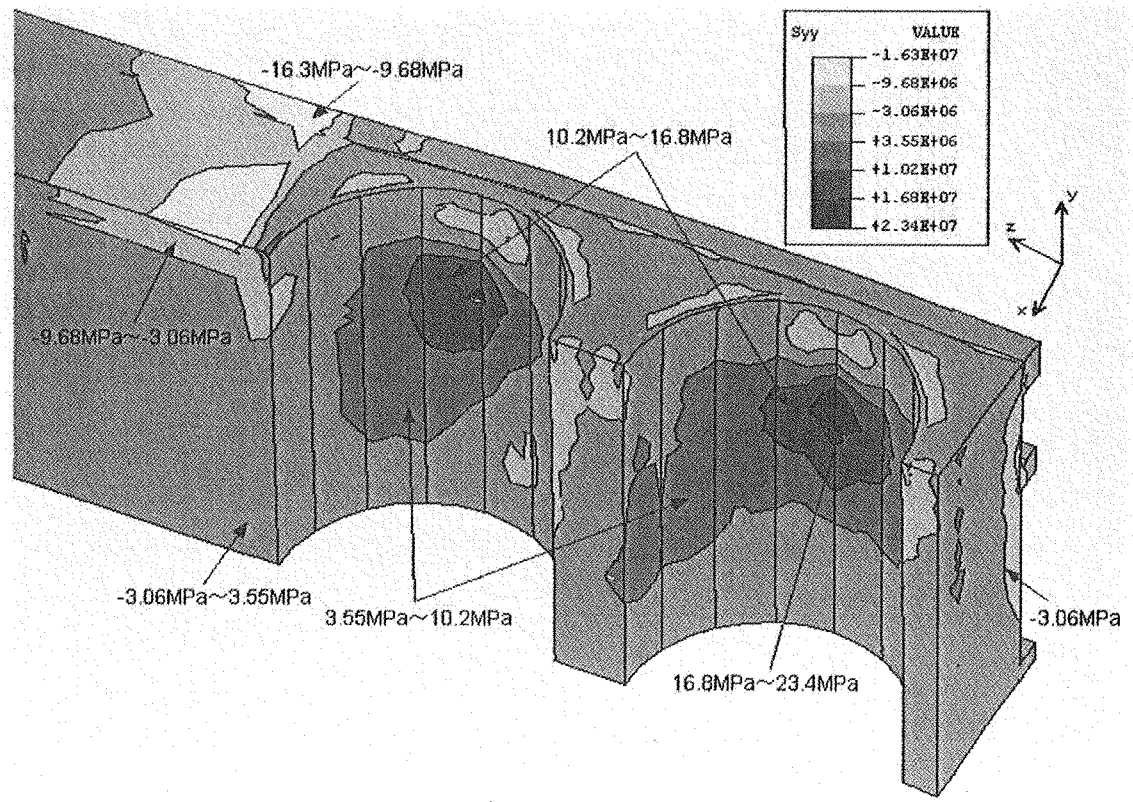

Figure 3.38 A close-up view of stress component (Syy). The heat flux distribution of case 1 was assumed.

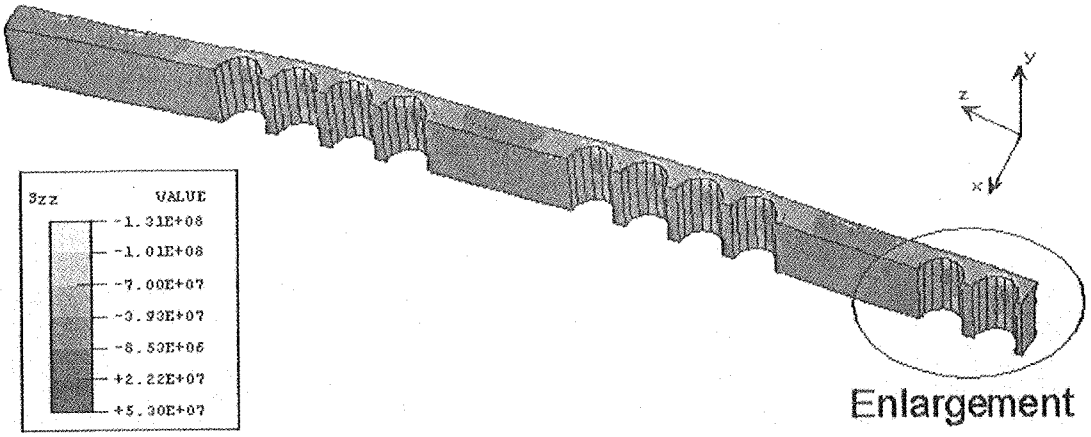

Figure 3.39 Stress component (Szz) for the heat loading of 1.5 MW. The heat flux distribution of case 1 was assumed.

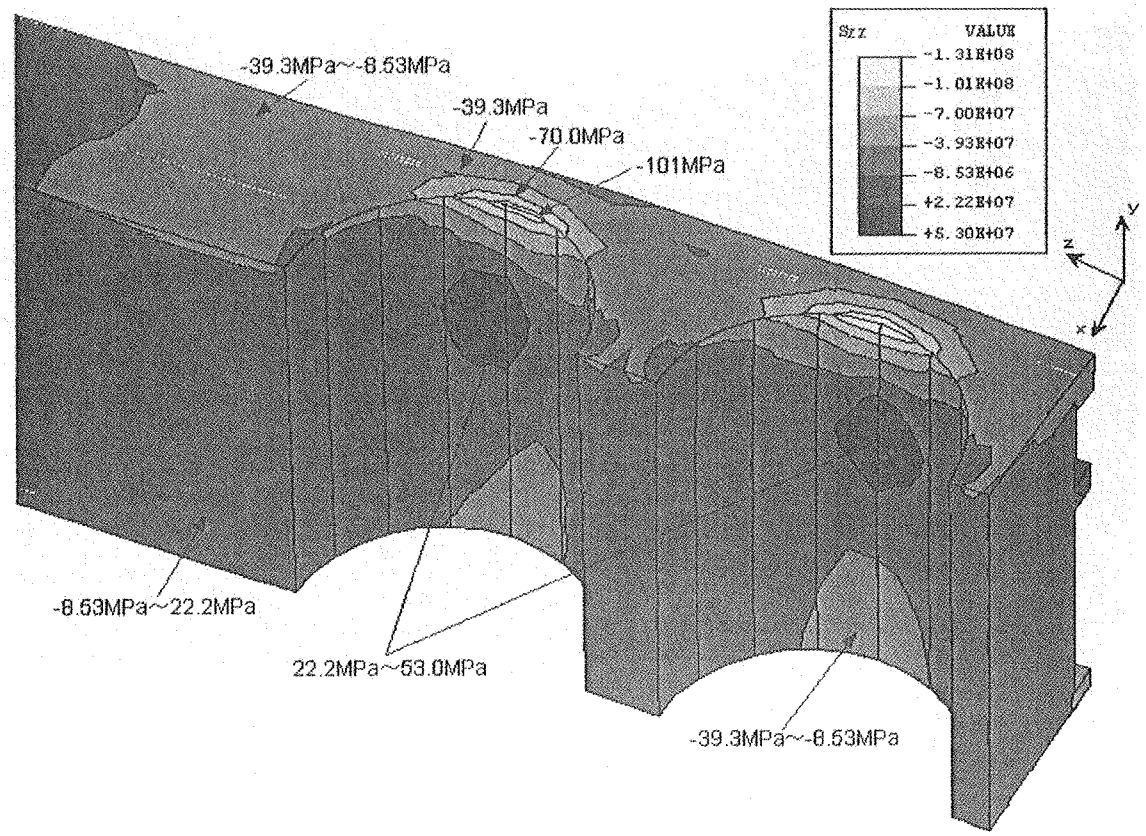

Figure 3.40 A close-up view of stress component (Szz). The heat flux distribution of case 1 was assumed.

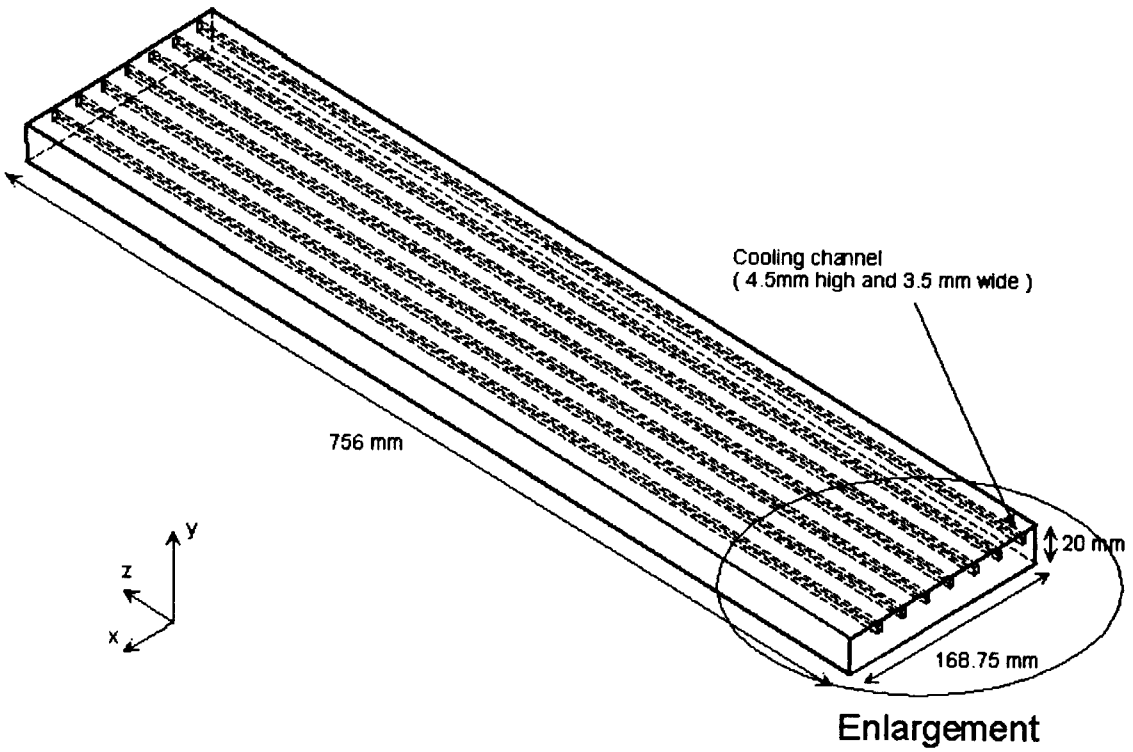

Figure 4.1 One-half model from a top view. One half of a single segment was selected as a computational region. Aperture regions were supposed to be made of a homogeneous material.

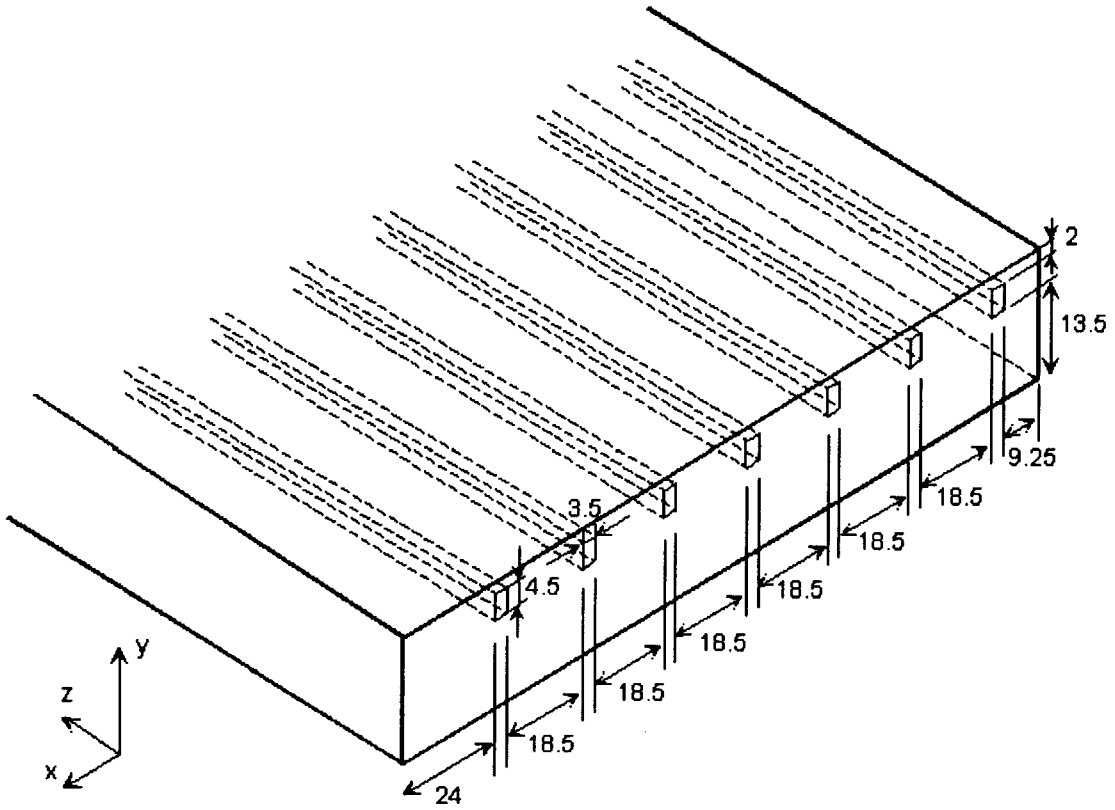

Figure 4.2 Detailed structure of the one-half model.

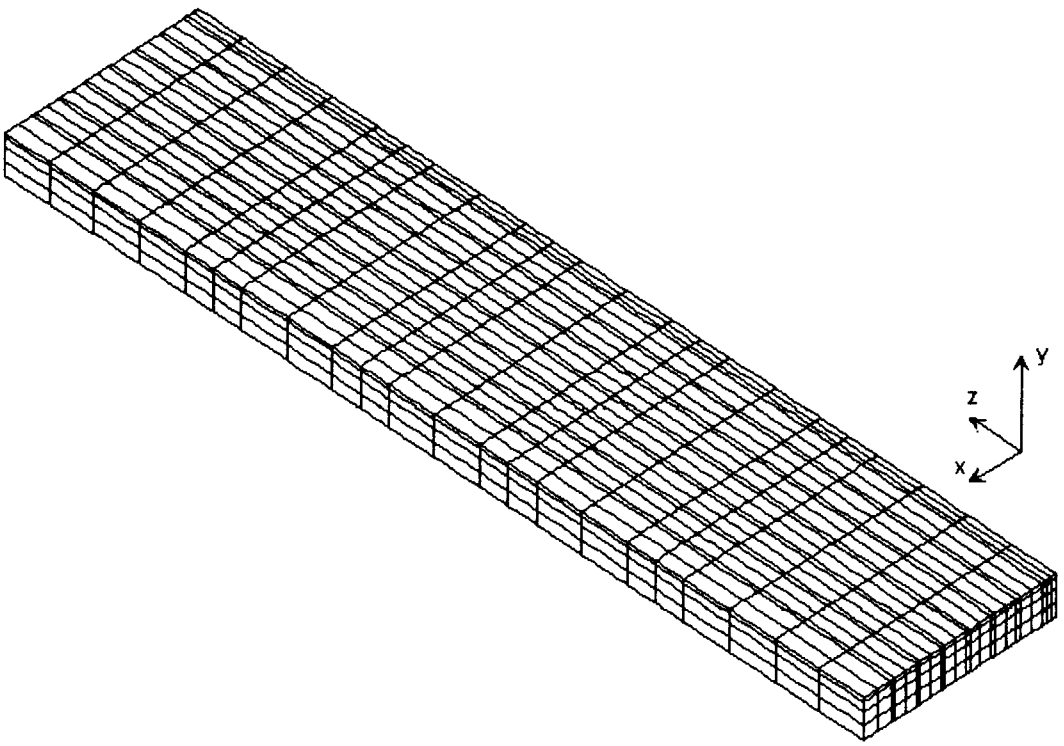

Figure 4.3 Finite element mesh of the one-half model from a top view.

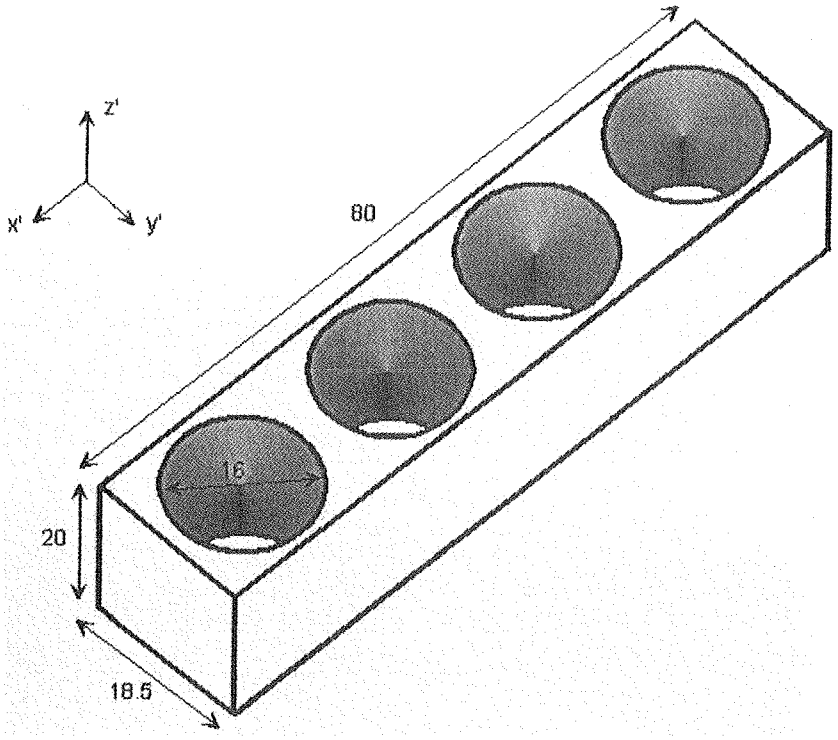

Figure 4.4 Mechanical properties of "four-aperture part" were evaluated using a three-dimensional simulation. The evaluated mechanical properties were utilized when the thermal deformation of the one-half model is calculated.

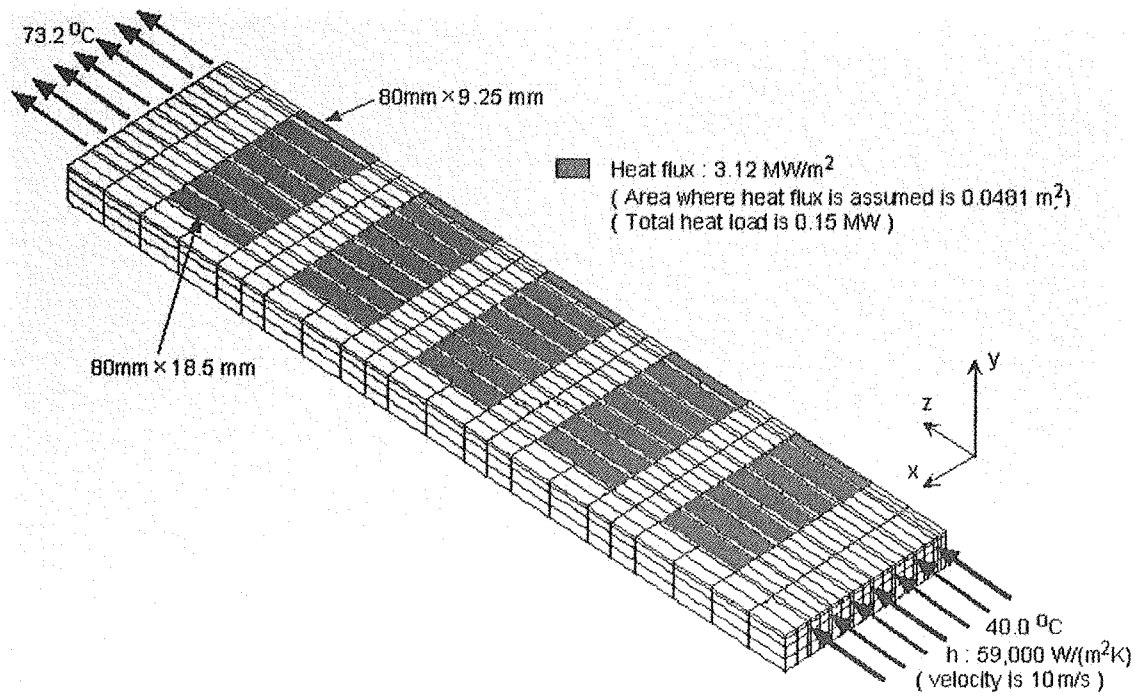

Figure 4.5 Boundary conditions for thermal analysis. Uniform heat flux of 3.12 MW/m^2 was assumed on the surfaces of the "four-aperture parts".

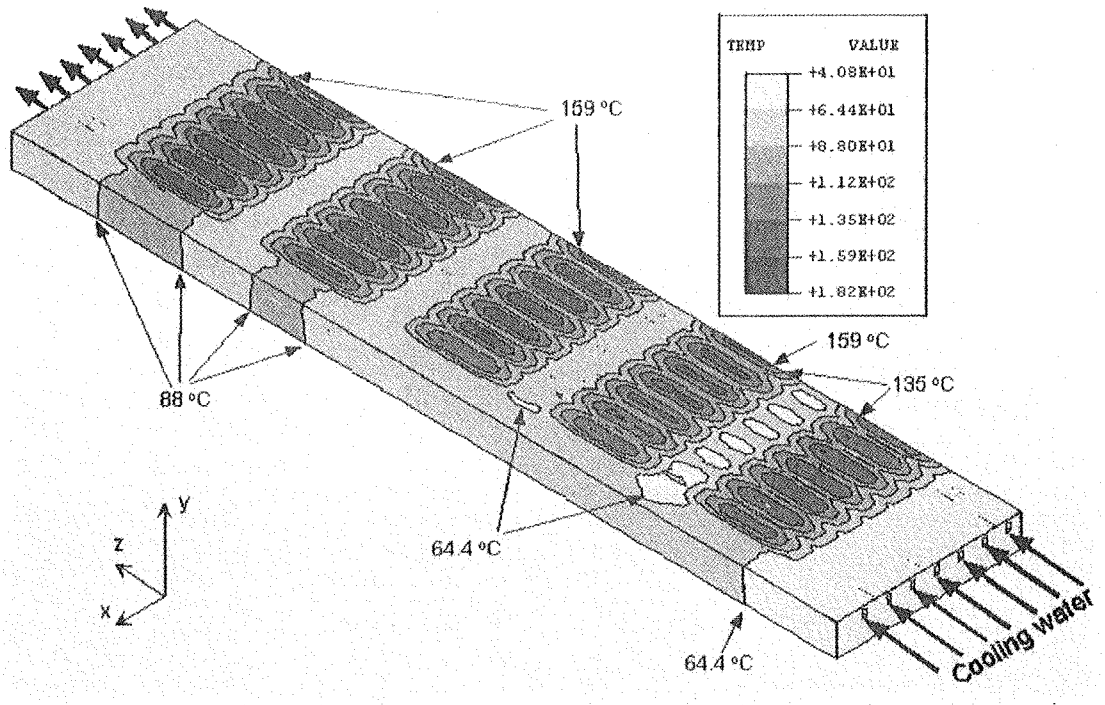

Figure 4.6 Temperature distribution from a top view for the heat loading of 1.5 MW. Inlet temperature of 40 °C and outlet temperature of 73.2 °C were assumed.

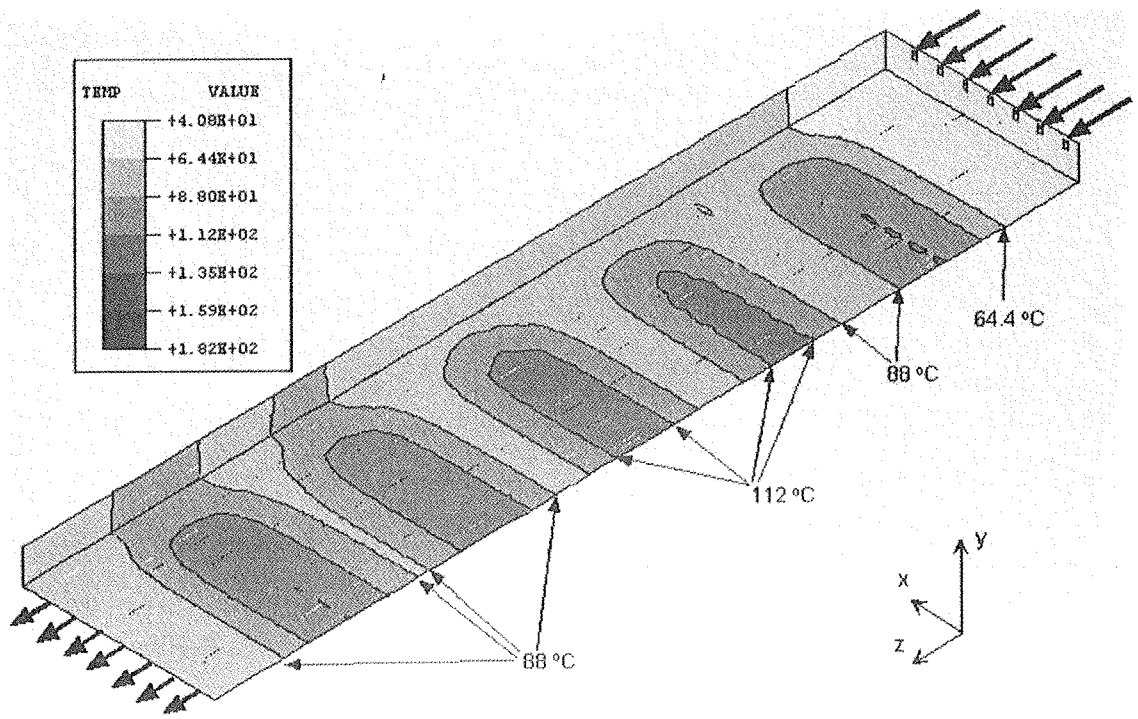

Figure 4.7 Temperature distributions from a bottom view.

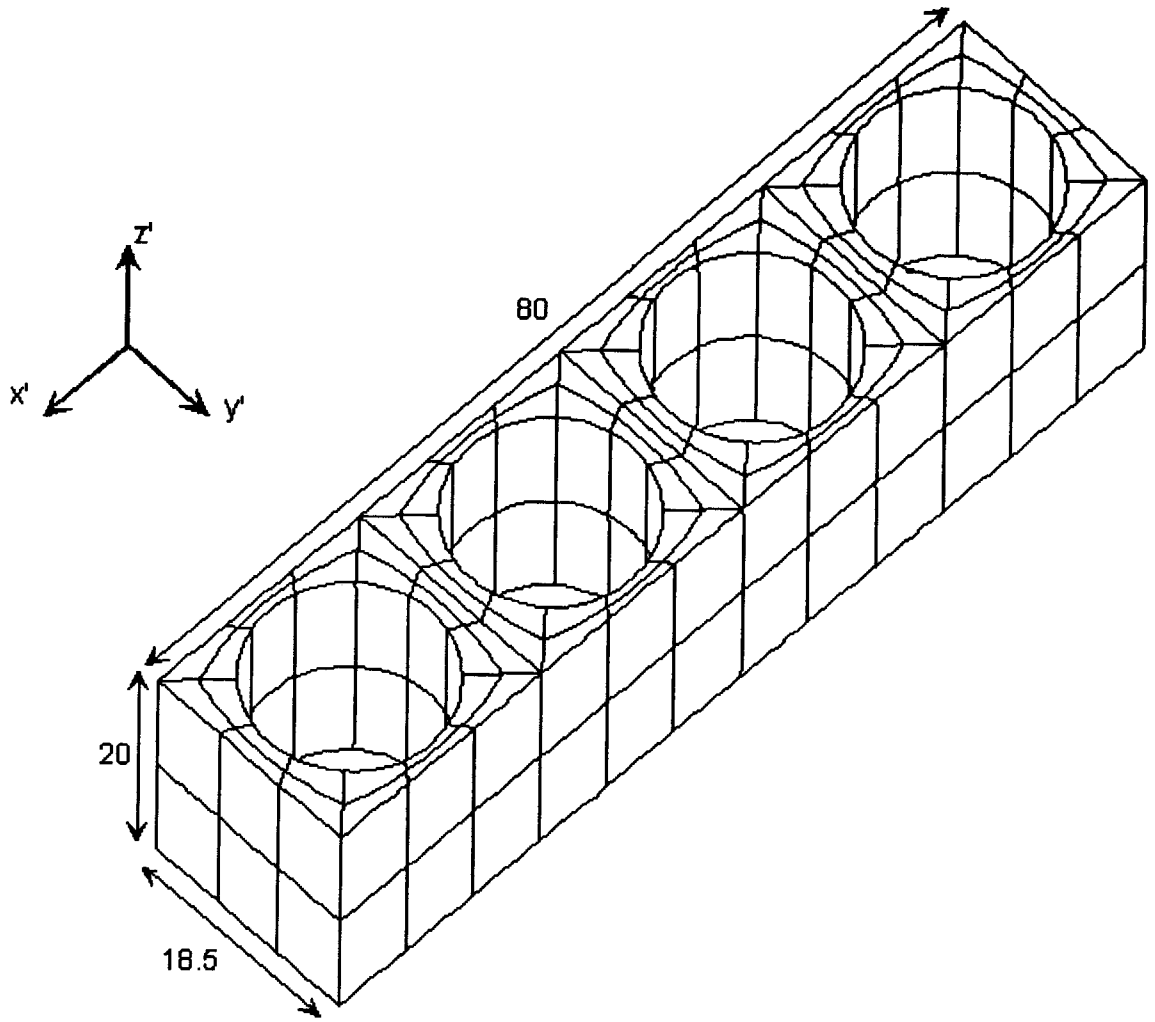

Figure 4.8 Finite element mesh of the "four-aperture part". The dimensions are 80 mm long, 18.5 mm wide and 20 mm high.

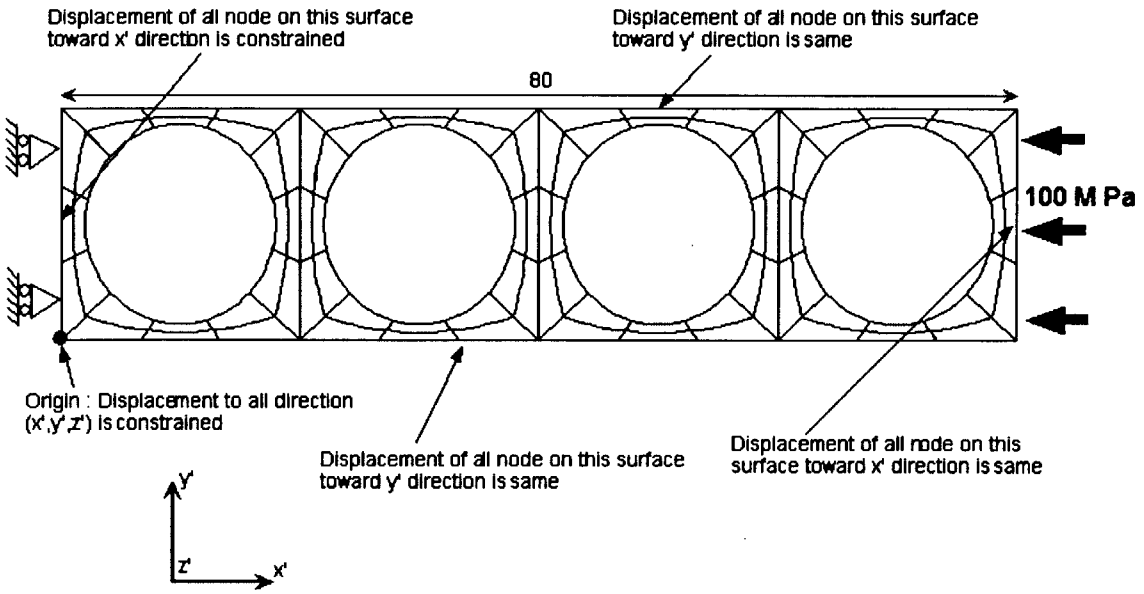

Figure 4.9 Boundary conditions for determining elastic modulus and poisson's ratio along x' direction. Pressure of 100 MPa was assumed to calculate displacement.

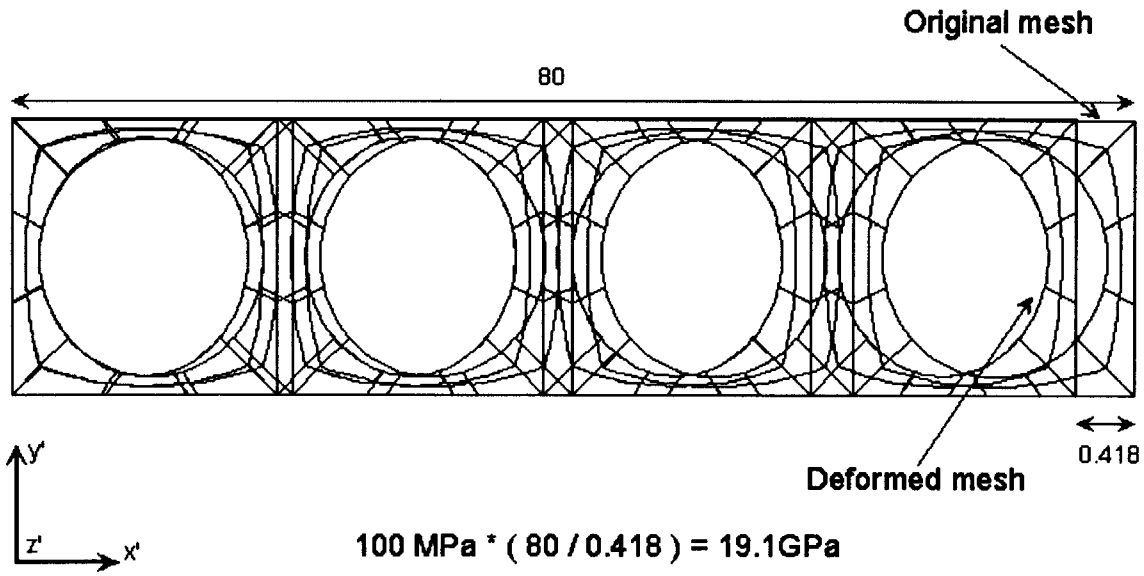

Figure 4.10 Calculated displacement. Deformation was enlarged by a factor of 10.

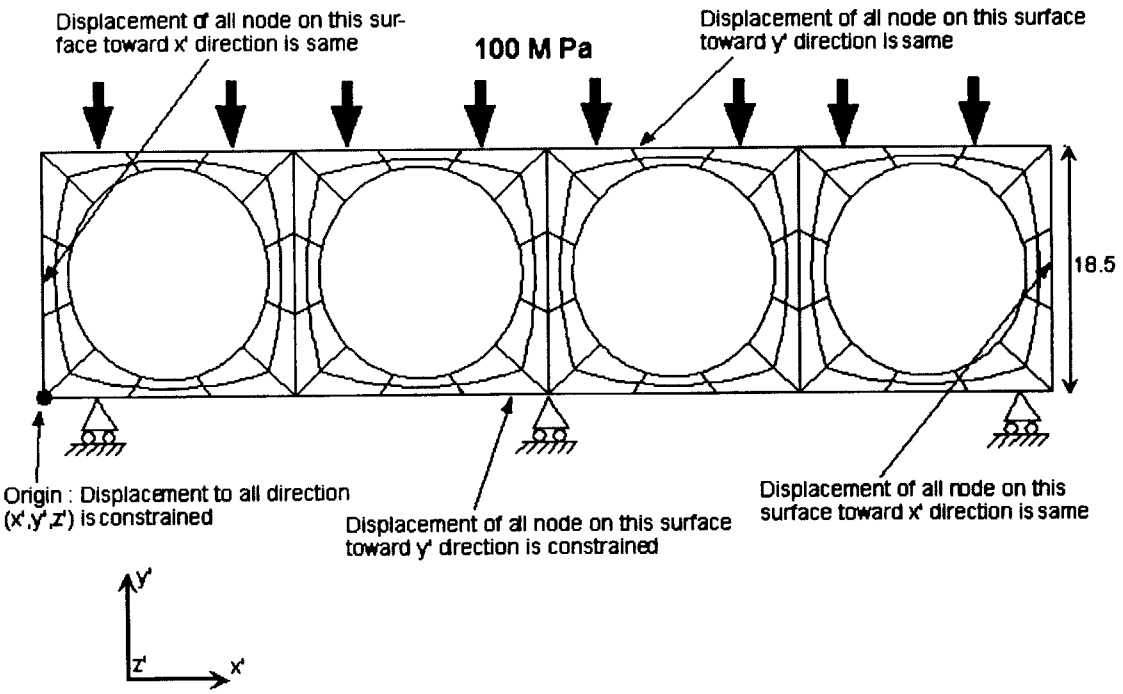

Figure 4.11 Boundary conditions for determining elastic modulus and poisson's ratio along y' direction. Pressure of 100 MPa was assumed.

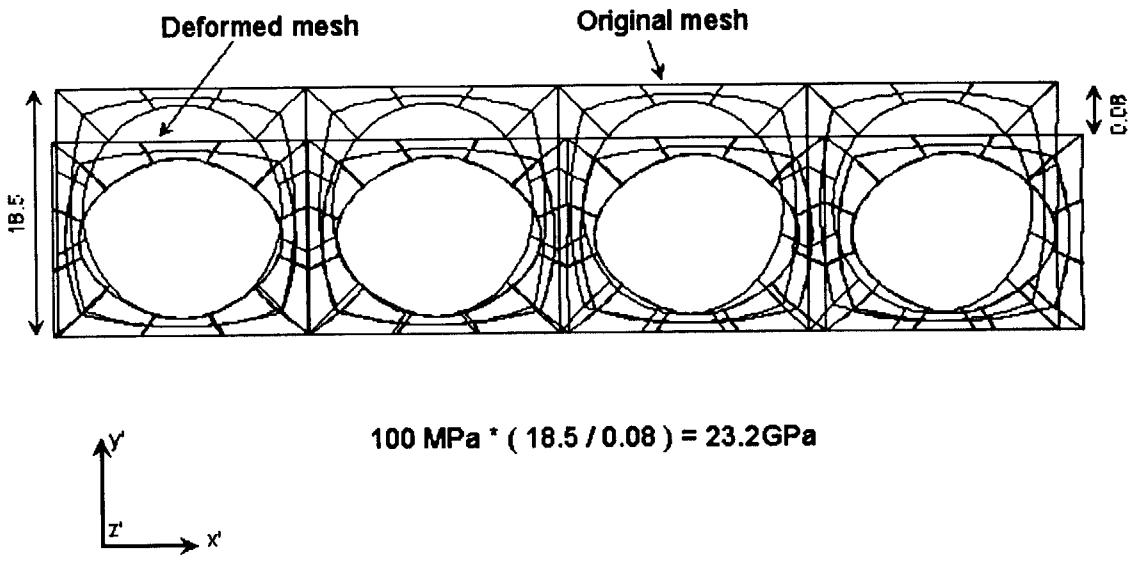

Figure 4.12 Calculated displacement. Deformation was enlarged by a factor of 50.

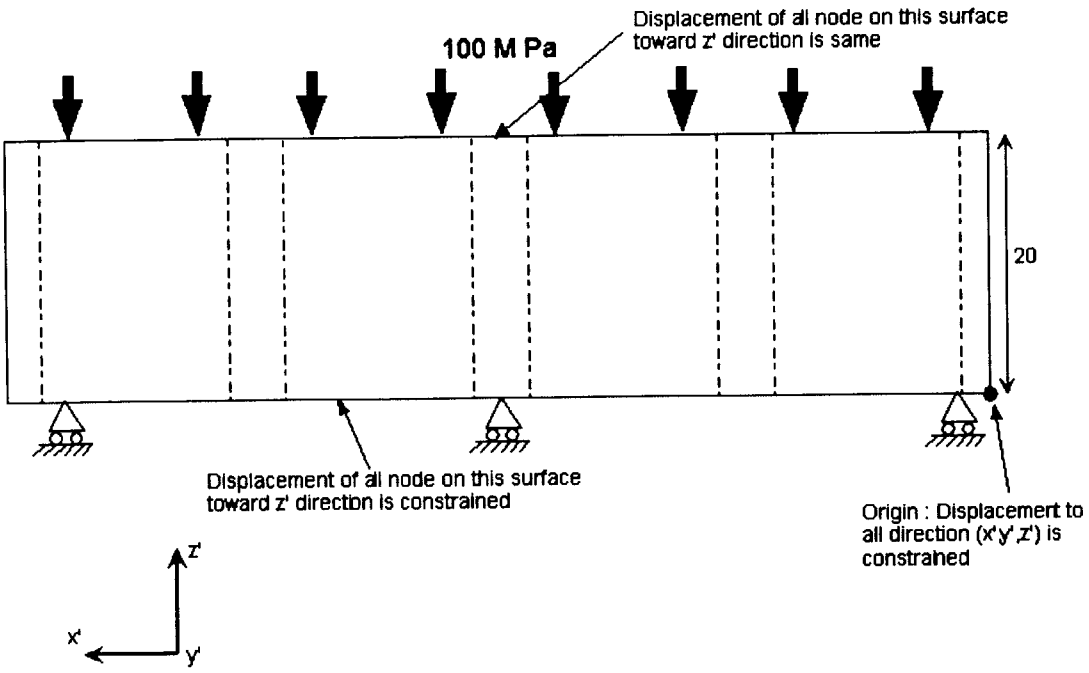

Figure 4.13 Boundary conditions for determining elastic modulus and poisson's ratio long z' direction. Pressure of 100 MPa was assumed.

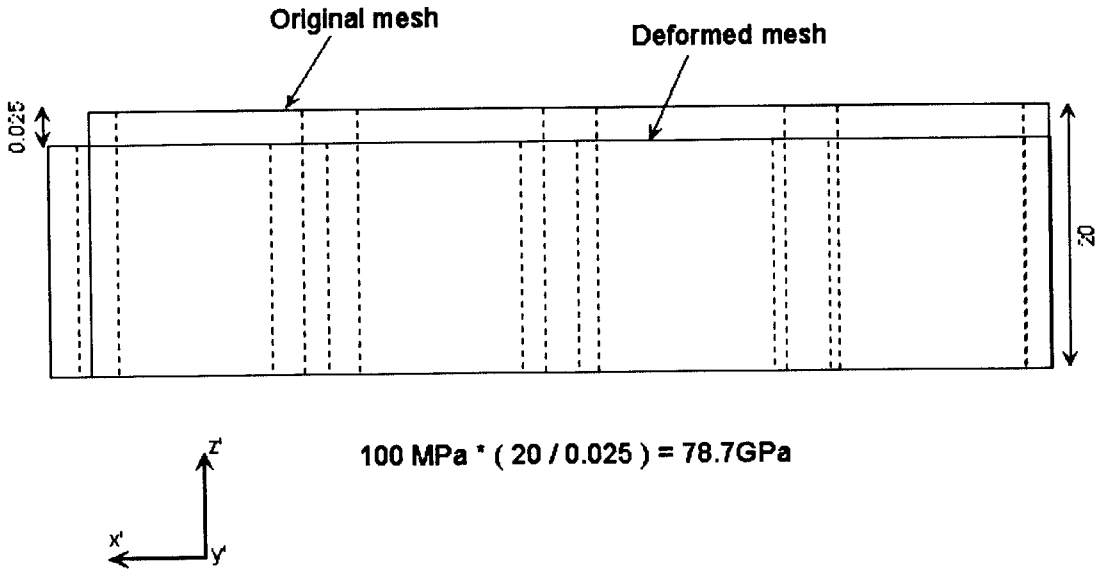

Figure 4.14 Calculated displacement. Deformation was enlarged by a factor of 100.

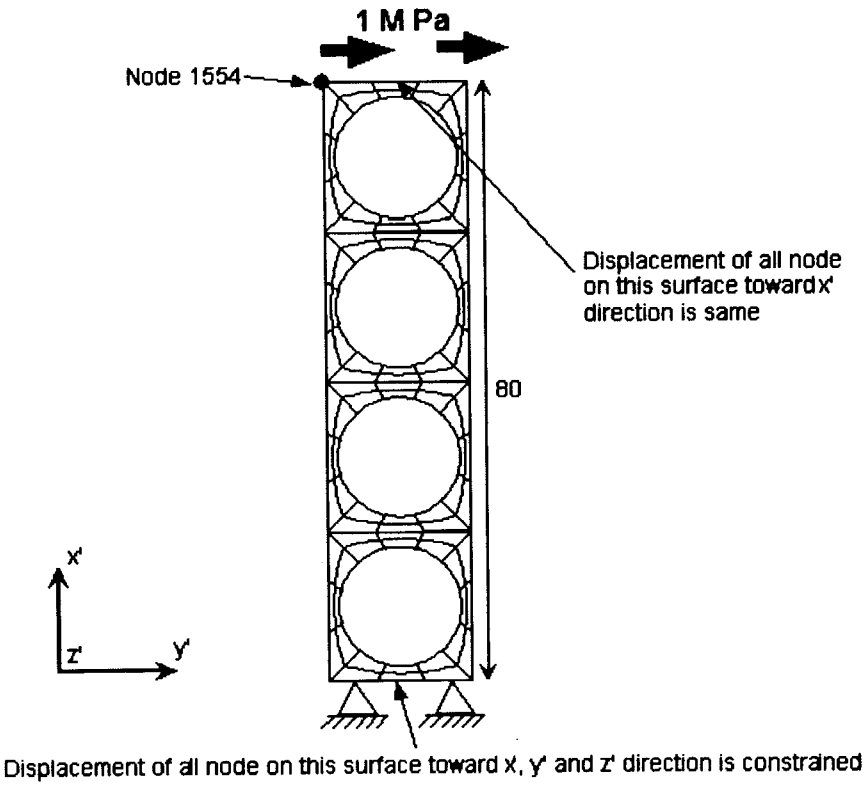

Figure 4.15 Boundary conditions for determining shear modulus along x'-y' direction. Pressure of 1 MPa was assumed to calculate displacement.

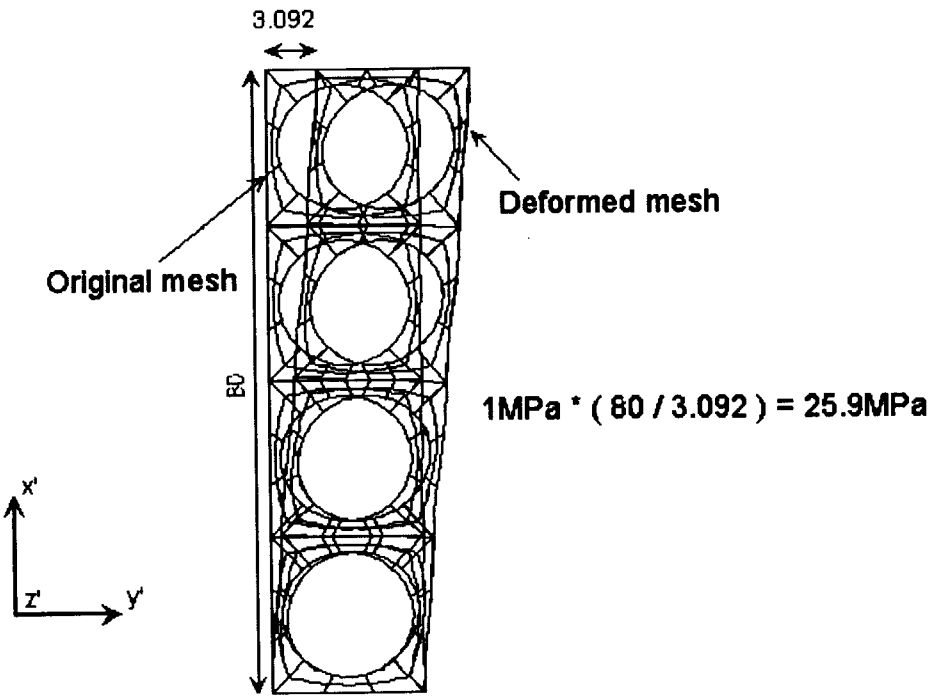

Figure 4.16 Calculated displacement. Deformation was enlarged by a factor of 2.

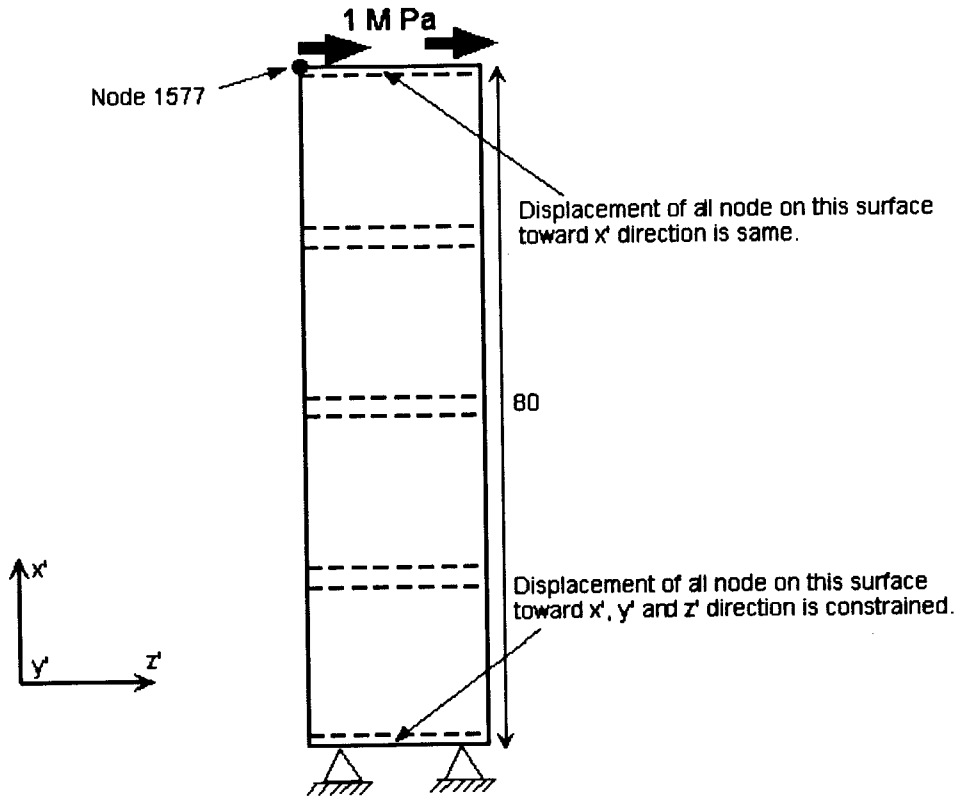

Figure 4.17 Boundary conditions for determining shear modulus along x'-z' direction. Pressure of 1 MPa was assumed to calculate displacement.

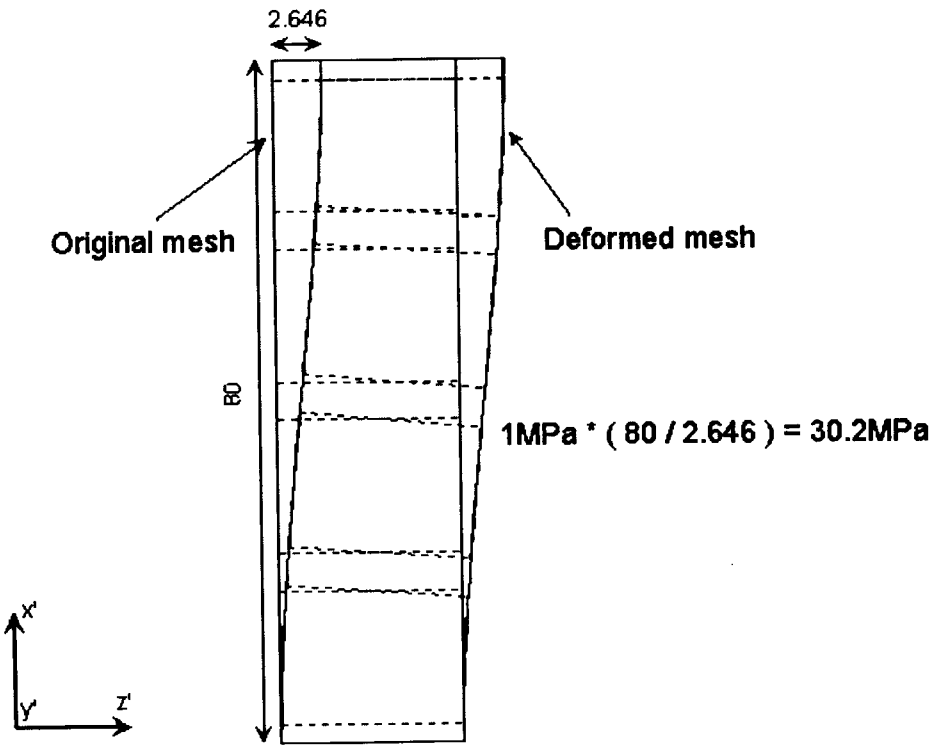

Figure 4.18 Calculated displacement. Deformation was enlarged by a factor of 2.

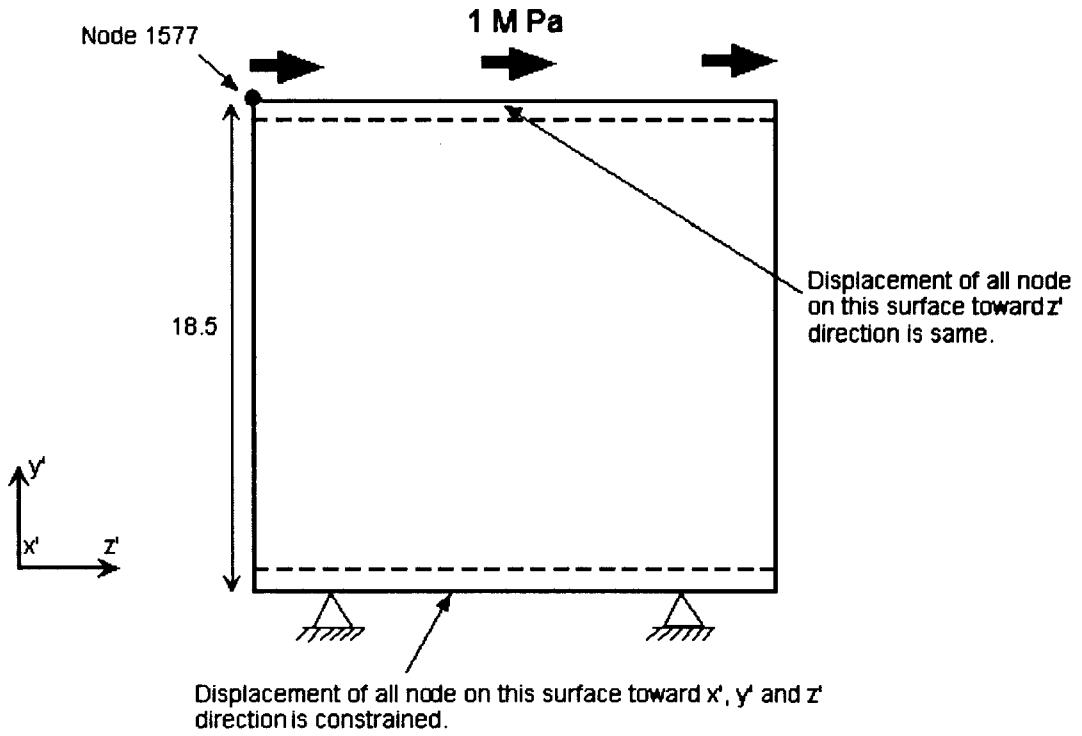

Figure 4.19 Boundary conditions for determining shear modulus along y'-z' direction. Pressure of 1 MPa was assumed to calculate displacement.

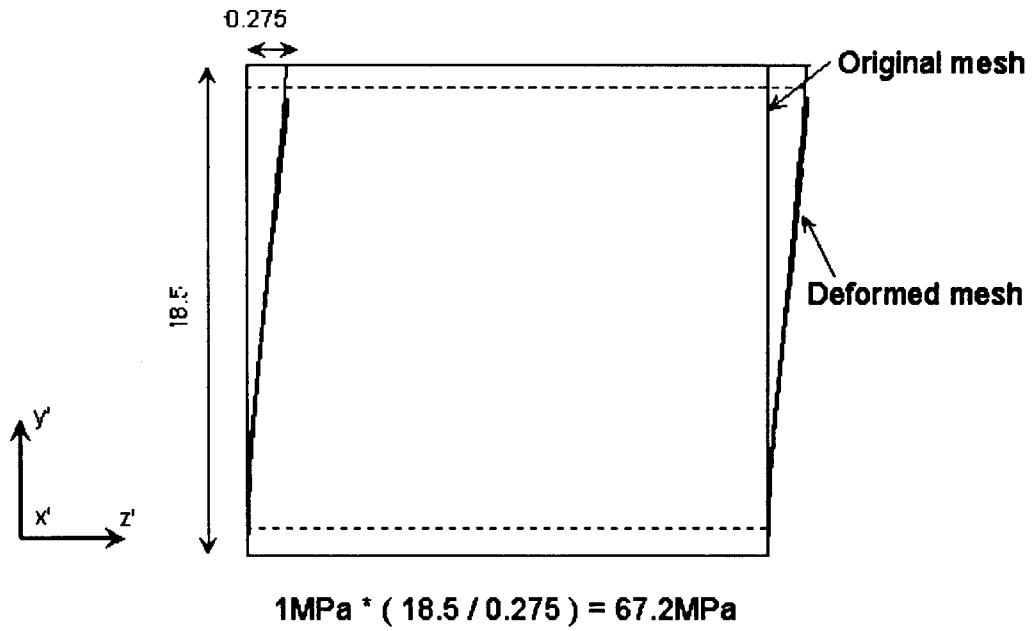

Figure 4.20 Calculated displacement. Displacement was enlarged by a factor of 5.

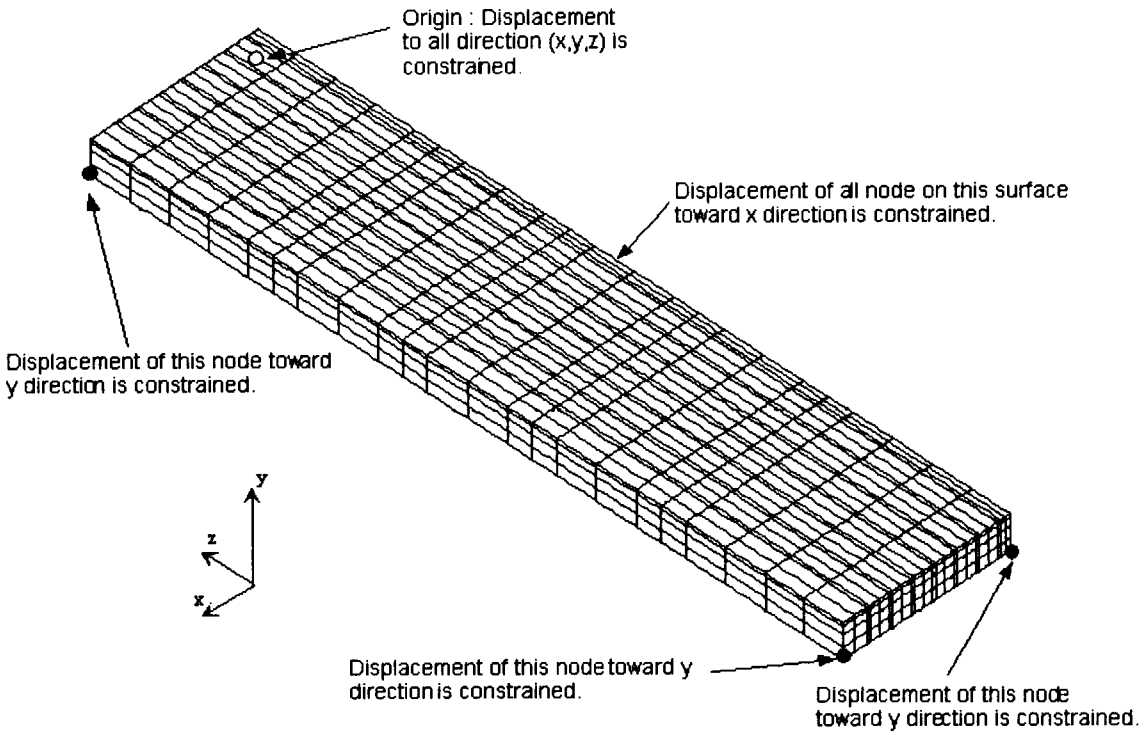

Figure 4.21 Boundary conditions for the elastic thermal analysis. The displacement of origin was assumed to be zero.

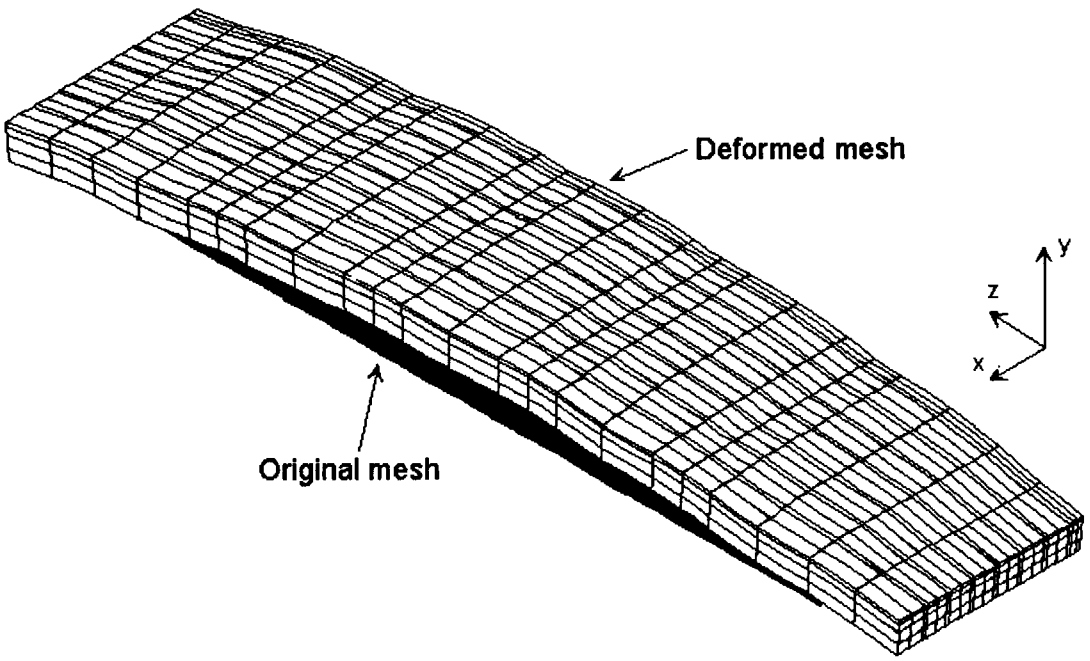

Figure 4.22 Node points and their displacement for the heat loading of 1.5 MW.

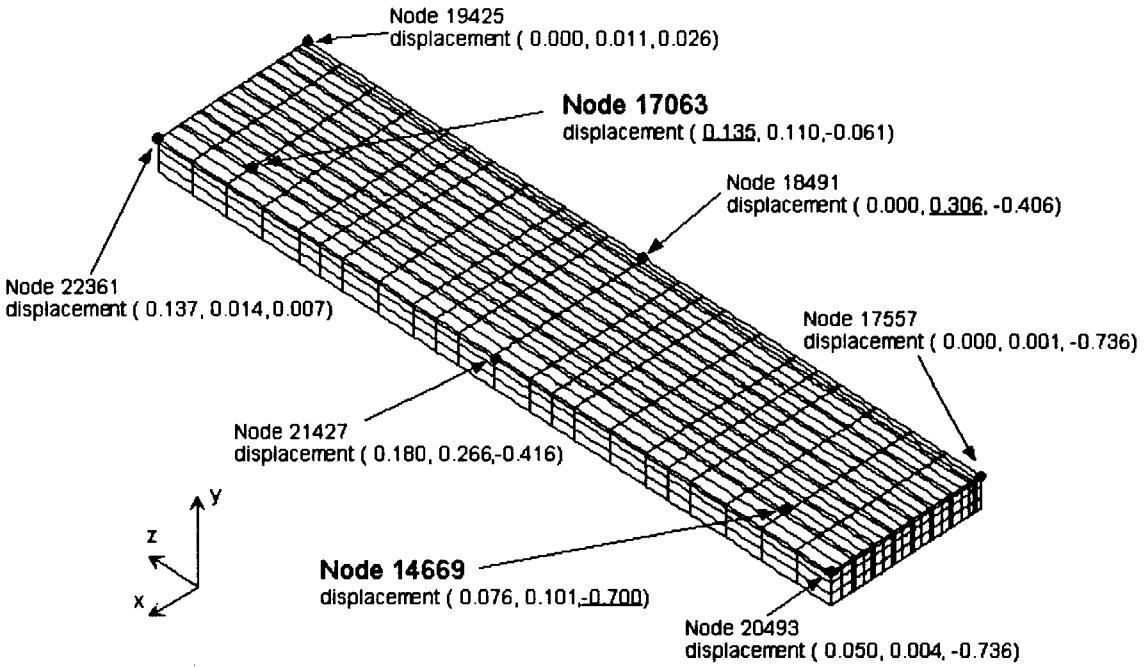

Figure 4.23 Thermal deformation from a front view enlarged by a factor of 100. Heat loading was assumed to be 1.5 MW.

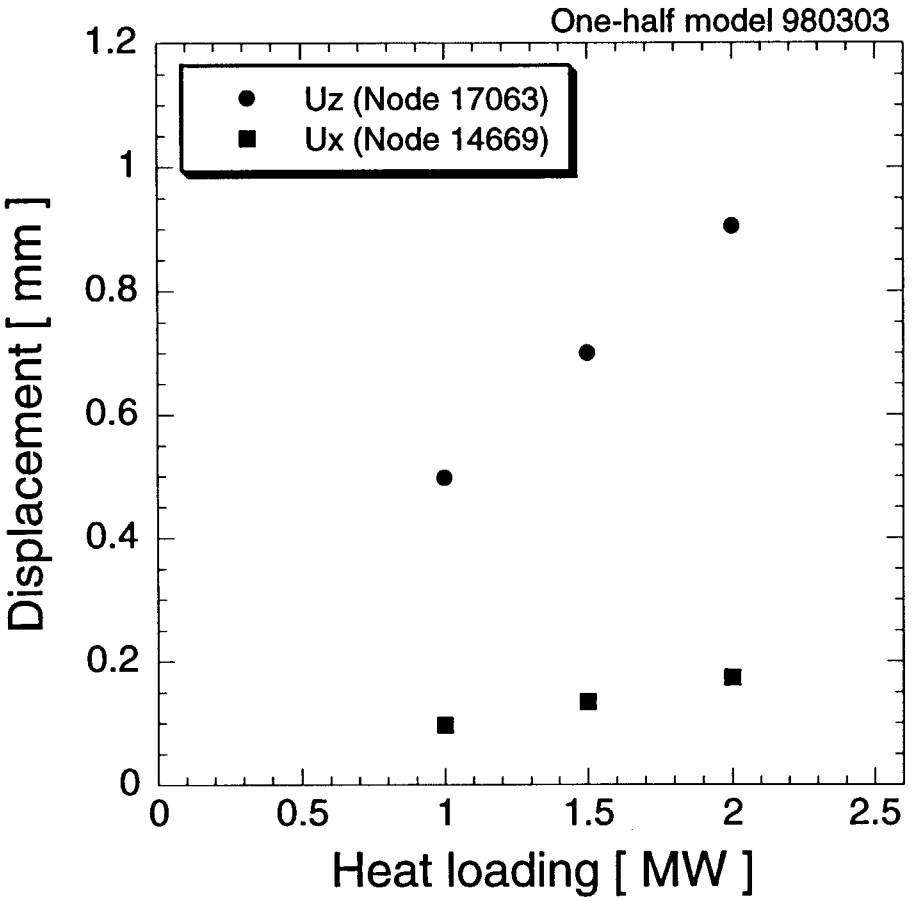

Figure 4.24 Maximum displacement as a function of heat loading.

国際単位系 (SI) と換算表

表1　SI基本単位および補助単位

量	名称	記号
長さ	メートル	m
質量	キログラム	kg
時間	秒	s
電流	アンペア	A
熱力学温度	ケルビン	K
物質量	モル	mol
光度	カンデラ	cd
平面角	ラジアン	rad
立体角	ステラジアン	sr

表2　SIと併用される単位

名称	記号
分，時，日	min，h，d
度，分，秒	°，′，″
リットル	l，L
トン	t
電子ボルト	eV
原子質量単位	u

1 eV = 1.60218 × 10^{-19} J

1 u = 1.66054 × 10^{-27} kg

表3　固有の名称をもつSI組立単位

量	名称	記号	他のSI単位による表現
周波数	ヘルツ	Hz	s^{-1}
力	ニュートン	N	$m\cdot kg/s^2$
圧力，応力	パスカル	Pa	N/m^2
エネルギー，仕事，熱量	ジュール	J	N·m
工率，放射束	ワット	W	J/s
電気量，電荷	クーロン	C	A·s
電位，電圧，起電力	ボルト	V	W/A
静電容量	ファラド	F	C/V
電気抵抗	オーム	Ω	V/A
コンダクタンス	ジーメンス	S	A/V
磁束	ウェーバ	Wb	V·s
磁束密度	テスラ	T	Wb/m^2
インダクタンス	ヘンリー	H	Wb/A
セルシウス温度	セルシウス度	℃	
光束	ルーメン	lm	cd·sr
照度	ルクス	lx	lm/m^2
放射能	ベクレル	Bq	s^{-1}
吸収線量	グレイ	Gy	J/kg
線量当量	シーベルト	Sv	J/kg

表4　SIと共に暫定的に維持される単位

名称	記号
オングストローム	Å
バーン	b
バール	bar
ガル	Gal
キュリー	Ci
レントゲン	R
ラド	rad
レム	rem

1 Å = 0.1 nm = 10^{-10} m

1 b = 100 fm^2 = 10^{-28} m^2

1 bar = 0.1 MPa = 10^5 Pa

1 Gal = 1 cm/s^2 = 10^{-2} m/s^2

1 Ci = 3.7 × 10^{10} Bq

1 R = 2.58 × 10^{-4} C/kg

1 rad = 1 cGy = 10^{-2} Gy

1 rem = 1 cSv = 10^{-2} Sv

表5　SI接頭語

倍数	接頭語	記号
10^{18}	エクサ	E
10^{15}	ペタ	P
10^{12}	テラ	T
10^{9}	ギガ	G
10^{6}	メガ	M
10^{3}	キロ	k
10^{2}	ヘクト	h
10^{1}	デカ	da
10^{-1}	デシ	d
10^{-2}	センチ	c
10^{-3}	ミリ	m
10^{-6}	マイクロ	μ
10^{-9}	ナノ	n
10^{-12}	ピコ	p
10^{-15}	フェムト	f
10^{-18}	アト	a

（注）

1. 表1－5は「国際単位系」第5版，国際度量衡局 1985年刊行による。ただし，1 eVおよび1 uの値はCODATAの1986年推奨値によった。
2. 表4には海里，ノット，アール，ヘクタールも含まれているが日常の単位なのでここでは省略した。
3. barは，JISでは流体の圧力を表わす場合に限り表2のカテゴリーに分類されている。
4. EC閣僚理事会指令ではbar，barnおよび「血圧の単位」mmHgを表2のカテゴリーに入れている。

換算表

力

N(=10^5 dyn)	kgf	lbf
1	0.101972	0.224809
9.80665	1	2.20462
4.44822	0.453592	1

粘度　1 Pa·s(N·s/m^2) = 10 P(ポアズ)(g/(cm·s))

動粘度　1 m^2/s = 10^4 St(ストークス)(cm^2/s)

圧力

MPa(=10 bar)	kgf/cm^2	atm	mmHg(Torr)	lbf/in^2(psi)
1	10.1972	9.86923	7.50062 × 10^3	145.038
0.0980665	1	0.967841	735.559	14.2233
0.101325	1.03323	1	760	14.6959
1.33322 × 10^{-4}	1.35951 × 10^{-3}	1.31579 × 10^{-3}	1	1.93368 × 10^{-2}
6.89476 × 10^{-3}	7.03070 × 10^{-2}	6.80460 × 10^{-2}	51.7149	1

エネルギー・仕事・熱量

J(=10^7 erg)	kgf·m	kW·h	cal(計量法)	Btu	ft·lbf	eV
1	0.101972	2.77778 × 10^{-7}	0.238889	9.47813 × 10^{-4}	0.737562	6.24150 × 10^{18}
9.80665	1	2.72407 × 10^{-6}	2.34270	9.29487 × 10^{-3}	7.23301	6.12082 × 10^{19}
3.6 × 10^6	3.67098 × 10^5	1	8.59999 × 10^5	3412.13	2.65522 × 10^6	2.24694 × 10^{25}
4.18605	0.426858	1.16279 × 10^{-6}	1	3.96759 × 10^{-3}	3.08747	2.61272 × 10^{19}
1055.06	107.586	2.93072 × 10^{-4}	252.042	1	778.172	6.58515 × 10^{21}
1.35582	0.138255	3.76616 × 10^{-7}	0.323890	1.28506 × 10^{-3}	1	8.46233 × 10^{18}
1.60218 × 10^{-19}	1.63377 × 10^{-20}	4.45050 × 10^{-26}	3.82743 × 10^{-20}	1.51857 × 10^{-22}	1.18171 × 10^{-19}	1

1 cal = 4.18605 J(計量法)
= 4.184 J　(熱化学)
= 4.1855 J　(15 °C)
= 4.1868 J(国際蒸気表)

仕事率　1 PS(仏馬力)
= 75 kgf·m/s
= 735.499 W

放射能

Bq	Ci
1	2.70270 × 10^{-11}
3.7 × 10^{10}	1

吸収線量

Gy	rad
1	100
0.01	1

照射線量

C/kg	R
1	3876
2.58 × 10^{-4}	1

線量当量

Sv	rem
1	100
0.01	1

（86年12月26日現在）

THERMO-MECHANICAL ANALYSIS OF AN ACCELERATION GRID FOR THE ITER-NBI SYSTEM